Preface

This master thesis is the final work in my study program of Chemical Engineering and Biotechnology at the Norwegian University of Science and Technology (NTNU). It is also a continuation of my specialization project *Synthesis of Lead-free Ferroelectric Tetragonal Tungsten Bronzes* from 2019.[1] Since I became increasingly interested in materials and their properties, it has been especially fascinating to learn more about their electrical properties. This complex field has baffled me since the beginning of my research. Thankfully, the wonderful research group Functional Materials and Materials Chemistry Research Group (FACET) has helped me gain insight into the field and I have learned a lot throughout the last year. I am also very grateful for the support from my supervisors professor Tor Grande and doctoral candidate Solveig Stubmo Aamlid. Tor is very knowledgeable within the field and always appraised my results and studied them with a keen eye. Solveig has extensive knowledge about the tetragonal tungsten bronzes and has been very helpful in the laboratory, teaching me the basics of practical ceramic engineering.

Abstract

The solid solution between the lead-free ceramic materials $Ba_4Na_2Nb_{10}O_{30}$ (BNN) and $K_4Bi_2Nb_{10}O_{30}$ (KBiN), with the tetragonal tungsten bronze structure, has been studied. The aim of the research was to look for a morphotropic phase boundary (MPB). The end members and four different ceramic solid solutions with a relative density above 90 % were made through a conventional solid-state synthesis method. The microstructure of the samples was imaged with a scanning electron microscope. X-ray diffraction was used to study the crystal structure and Pawley refinement was applied to find the evolution of the lattice parameters. Dielectric spectroscopy was used to measure the dielectric permittivity as a function of temperature and frequency. The dielectric data showed that the critical temperature decreases with increased mixing of the end members. In addition, the KBiN rich samples of the solid solution have broad dielectric peaks typical of relaxor behaviour and Uchino analysis supports this observation. Based on enhanced dielectric permittivity and a significant change in both the a and c lattice parameters, a MPB is proposed to exist in the solid solution at a composition of 0.6BNN-0.4KBiN.

Sammendrag

Faststoffløsningen mellom de to blyfrie keramiske materialene med tetragonal wolframbronse-struktur, $Ba_4Na_2Nb_{10}O_{30}$ (BNN) og $K_4Bi_2Nb_{10}O_{30}$ (KBiN), ble studert. Studiens mål var å lete etter en morfotropisk faseovergang. Sluttmedlemmene og fire forskjellige faststoffløsninger ble syntetisert via en standard sintringsmetode og oppnådde en relativ tetthet over 90 %. Mikrostrukturen ble undersøkt ved hjelp av et elektronmikroskop. Røntgendiffraksjon ble brukt for å undersøke krystallstruktur og utviklingen til gitterkonstantene ble funnet ved hjelp av Pawley-raffinering. Dielektrisk spektroskopi ble brukt for å måle dielektrisk permittivitet som en funksjon av temperatur og frekvens. De dielektriske dataene viste at den kritiske temperaturen synker med økt blandingsforhold av endefasene. I tillegg har faststoffløsningene som er rike på KBiN brede dielektriske topper som er typisk for relaxor-oppførsel, og Uchino-analyse støtter denne observasjonen. Basert på økt dielektrisk permittivitet og en betydelig endring i både *a*- og *c*-gitterkonstantene, foreslås en morfotropisk faseovergang ved en sammensetning på 0.6BNN-0.4KBiN.

Contents

1 Introduction

1.1 Background

Tetragonal tungsten bronzes (TTB) is an important category of oxide materials with a similar crystal structure, first described by Magnéli in 1949. [2] The structure is intricate and is known to exhibit certain functional properties, like ferroelectricity. This can occur because the structure is able to undergo complex distortions like rotation of oxygen octahedra, causing modulated superstructures. [3] As the structure can accommodate many different species, it gives a wide variety of material compositions and doping possibilities, many of which have not been thoroughly researched before. The ferroelectric properties make the TTBs very interesting with regards to technological applications, like that based on ultrasound generation and detection. The field of ferroelectric materials research is currently searching for new lead-free candidate materials with properties warranting the replacement of existing hazardous lead-containing materials. [4]

The possible complex composition and chemical crystal structure is both an advantage and disadvantage for the TTB system. It means that the system is difficult to both control and investigate, but there are also many possible mechanisms for functional properties to arise. At the Norwegian University of Science and Technology (NTNU), there has been a research incentive based around the TTB structure, both in simulation and experimental research. This master project is a contribution to this research. Examples of prior work on this subject include doctoral candidate Aamlid's investigation on strontium barium niobate [5] and barium sodium niobate. [6] Olsen also wrote his doctoral thesis on the TTB system in 2016 at NTNU. [7]

Additionally, a preliminary study was performed by the author in 2019, in which dense and phase pure potassium bismuth niobate (KBiN) and barium sodium niobate (BNN) samples with the TTB crystal structure were synthesized. [1] A high temperature x-ray diffraction (HTXRD) scan from room temperature up to 700 °C indicated that KBiN loses a few low intensity x-ray diffraction (XRD) lines upon heating, pointing towards a prior undetermined phase transition to a different space group. It also showed that KBiN experiences a discontinuity in the thermal expansion of the a lattice parameter, but not in the c direction. This can be interpreted

as if KBiN has a polarization in the *ab* plane. As it is known that BNN has out-of-plane polarization, this reinforced the hypothesis that a morphotropic phase boundary (MPB) exists in a solid solution between KBiN and BNN.

1.2 Aim of the work

The aim of this master thesis was to make and investigate the solid solution between KBiN and BNN. The primary focus was to find a MPB, as well as measuring the dielectric properties of the solid solution system. The first part of the work consisted of making dense and phase pure samples. Afterwards, structural investigations were conducted with XRD and dielectric properties were measured by dielectric spectroscopy. The data was used to draw conclusions about the critical temperature and phase transitions in the system.

2 Literature Review

A basic understanding of ferroelectricity can be attained from reading general textbooks on the subject. If not otherwise stated, facts from the literature review can be found in one of the following textbooks: *Understanding Solids* [8] by Tilley *et al.*, *Solid State Chemistry* [9] by West or *Modern Ceramic Engineering* by Richerson and Lee. [10]

2.1 Ferroelectrics

Ferroelectric materials are a subgroup of electrically insulating materials known as dielectrics. An ideal dielectric material should have zero electrical conductivity. When a dielectric is exposed to the charge of an electric field, a charge separation termed polarization occurs in the material. This happens because the material is unable to remove the charge by conduction and therefore forms an opposing electrical dipole to reduce the magnitude of the forces it is subjected to. Polarization can arise in the material through multiple different mechanisms, depending mostly on the material, temperature and the frequency of the applied electric field.

As well as being electrically insulating, ferroelectric materials must fulfill three additional conditions. Firstly, they are piezoelectric, meaning that the material polarizes when subjected to mechanical stress. Conversely, when an electric field is applied, the polarization created in the material causes a change in its physical shape, thereby straining it. Piezoelectric materials have to lack inversion symmetry, a condition which reduces the possible crystal systems that can be ferroelectric to 21 point groups.

The second condition is that ferroelectrics are pyroelectric. A pyroelectric material is defined as having a natural and spontaneous polarization below a temperature threshold. It means that the polarization is present in the material even without the application of an electrical field. This causes the material to generate a voltage upon heating or cooling, as the magnitude of the spontaneous polarization changes as a function of the temperature. Only materials with a unique polar axis have this property, further reducing the possible ferroelectric crystal systems to 10 point groups.

The third and final condition is that the spontaneous polarization in ferroelectric materials can be switched by applying an electric field with the

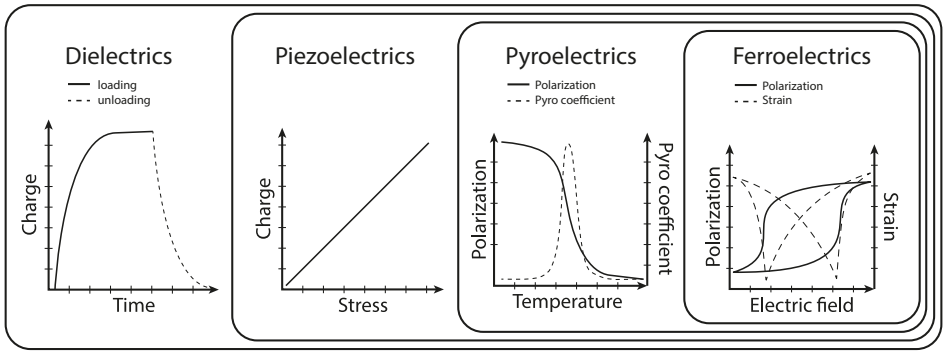

Figure 2.1: Set diagram showing the relationship between the different classes of dielectrics and some of their characteristic reactions to the application of different forces.

opposite charge direction, making the polarization reversible. That way, ferroelectric materials support two stable and switchable states. This in turn cause them to display a hysteresis with respect to the applied electrical field. For a material to be ferroelectric, it requires a structure with a unique polar axis with two distinct minima. This cannot be discerned by space groups alone, but require other means of testing to determine. Another characteristic property is the strain response to electric field, which looks like butterfly wings when plotted.

These three conditions separate the dielectric materials into four progressively smaller subgroups or classes. The relationship can be neatly presented in a set diagram, shown in figure 2.1. All of these properties open up for different and interesting applications in which ferroelectric materials can be used.

2.2 Origin of Polarization

As stated in section 2.1, ferroelectric materials polarize under the influence of an electric field, dependent on the material composition and structure, as well as the electric field's frequency. The electric field affects the position of electrons, atoms, ions and dipolar molecules in the material. It is the movement of these charged species that contribute to the total macroscopic polarization.

The polarization can be measured by conducting a dielectric analysis. This is done by alternating the frequency and temperature over a parallel plate capacitor. From the capacitance measured, the property known as dielectric permittivity, $\epsilon^{'}$, is acquired. The formula is given in equation 2.1, where C_1 is the capacitance of the sample and C_0 is the capacitance of vacuum. The capacitance of a sample is given in equation 2.2, where A is the area of the parallel plates and d is the distance between them. This can also be described in terms of the charge, Q_0, and voltage, V.

$$\epsilon^{'} = \frac{C_1}{C_0} \tag{2.1}$$

$$C_1 = \frac{\epsilon^{'} A}{d} = \frac{Q_0}{V} \tag{2.2}$$

The dielectric permittivity is often used to describe a dielectric material and is also related to the terms dielectric susceptibility and polarization. All the variables share the same origin, but each have slightly different definitions. Equation 2.3 shows the connection between them. P is the macroscopic polarization, ϵ_0 is the permittivity of vacuum, χ is material specific dielectric susceptibility and E_0 is the applied electric field.

$$P = \epsilon_0 \chi E_0 \tag{2.3}$$

2.2.1 Frequency Dependency

The dielectric permittivity generally decreases with an increase in frequency. This is attributed to the fact that lower frequencies allow polarization of more species in the material. At the fastest frequencies in the ultraviolet and visible spectrum, only small displacements of the electron clouds have time to align and oppose the applied electric field. This is called electronic polarization. At frequencies in the infrared range, ions in the crystal lattice have time to displace, adding to the permittivity as ionic polarization. This is the polarization that is most interesting in ferroelectrics and will be discussed further in section 2.2.2. Lowering the frequency even more gives dipolar molecules the time required to reorient against the applied field. This is called dipolar orientational polarization.

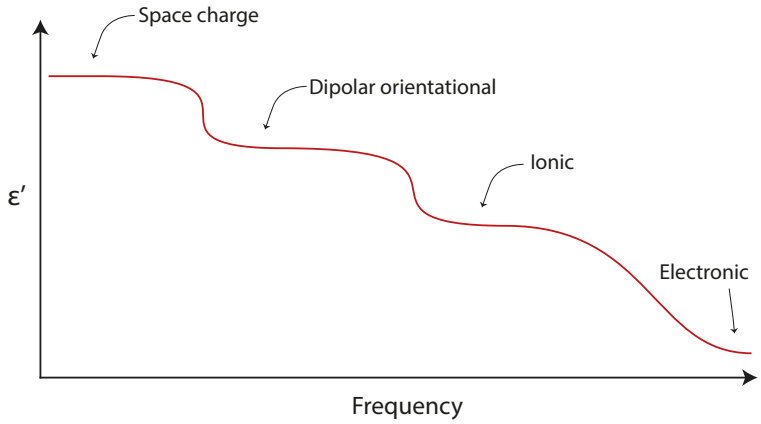

Figure 2.2: Frequency dependence of the different polarization mechanisms that contribute to the dielectric permittivity, ϵ'.

The slowest polarization mechanism is found at the lowest frequency ranges in the audio and radio wavelengths. It is called space charge polarization and consists of any long-range ordering of ionic or electronic species in the material. An example of this is ionic species in solution migrating through the material and gathering at the electrodes. All the different polarization mechanisms can be summarized in a plot of the permittivity against frequency, as shown in figure 2.2. A jump in the value of the dielectric permittivity corresponds to the onset or disappearance of a polarization mechanism. The different contributions from the polarization mechanisms is apparent as new plateaus in the diagram.

2.2.2 Distortions and Displacement

As previously described, an important property for ferroelectrics is its polarization mechanism. To form an opposing charge, charged species must move or occupy positions away from a symmetrical position. In ferroelectric materials, this usually happens on the microscopic scale by the movement of charged species in the crystal lattice. This can happen by distortions or displacements. One of the better known examples is the perovskite structure barium titanate (BTO). The paraelectric and ferroelectric crystal structure of BTO is shown in figure 2.3. The crystal structure of

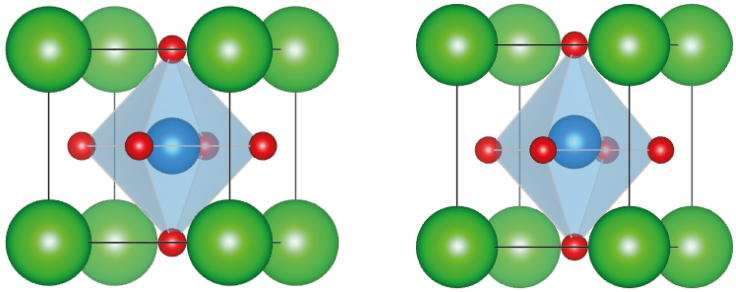

Figure 2.3: Crystal structures of barium titanate. The left unit cell shows the paraelectric cubic structure, while the right shows the tetragonal ferroelectric phase with the Ti^{4+} atom displaced along the polar c axis. Note that the displacement of Ti^{4+} also affects O^{2-} and causes an elongation of the c axis, which is exaggerated in the figure. The models were made with the VESTA software.[12]

BTO has a Ti^{4+} atom surrounded by an oxygen octahedron in a grid of Ba atoms. The charged titanium atom can be displaced and preferentially bond with some of the surrounding oxygen atoms. This displacement of the atom is the cause of polarization in the material.[11] This is a classic example of how an atom can be displaced and is valid for many perovskites, for example lead titanate.

2.2.3 Temperature Dependence: The Critical Temperature

The displaced atom allowing polarization is only stable in two positions below a certain temperature. Increasing the temperature leads to increased kinetic energy which broadens the two stable positions of the atom. At a certain temperature, the two positions merge into one, removing the atom's ability to polarize the material. The temperature where this occurs is called the critical temperature, T_C. It is also known as the Curie temperature.

Above the critical temperature, ferroelectrics generally follow the Curie-Weiss behaviour given in equation 2.4, where ϵ_r is the relative dielectric permittivity, C is a material specific constant, T is the absolute temperature and T_C is the critical temperature. The Curie-Weiss law predicts an anomaly in the dielectric permittivity at the critical temperature.

$$\epsilon_r(T) = \frac{C}{T - T_C} \tag{2.4}$$

2.3 Phase Transitions

A phase transition is used to refer to a change in a material's state, which is related to a change in properties. One specific example is when a ferroelectric material changes from the paraelectric to the ferroelectric state. This is accompanied by changes in other properties, like crystal structure and thermal expansion. Because of this, the transition can be measured by multiple different methods, depending on which property changes.

A couple of relevant examples are x-ray diffraction, thermal expansion and dielectric permittivity. When a material changes crystal structure, the x-ray diffraction pattern changes. From analysing the HTXRD crystallographic data, it is also possible to see how the lattice parameters change and a measure of the thermal expansion from before and after a transition can be found. This can also be measured using dilatometry. For ferroelectric samples, phase transitions are characterized by a change in their dielectric properties. Most noticeably, the transition from ferroelectric to paraelectric state is accompanied by a peak in dielectric permittivity and in dielectric loss. A ferroelastic transition can also be seen in such analysis, but it is a smaller and less noticeable difference. The magnitude of change in each property is different for each material and the type of transition. Because of this, different measurement methods must be used for different transitions. While a ferroelectric to paraelectric phase transition is easy to spot using dielectric spectroscopy, it can be much more subtle in a x-ray diffraction pattern.

The ferroelectric phase transition is either a displacive or order-disorder transition, or a combination. In a displacive phase transition, the bonds change length and direction without breaking or forming bonds. This can also cause shearing or tilting of polyhedra. This can result in the two stable minima along the polar axis described previously when discussing ferroelectricity in section 2.1 and displacement in section 2.2.2. Order-disorder transitions happen in materials that are entropy-stabilized. In an order-disorder ferroelectric material, long-range electrostatic forces overcome the energy contribution of the disorder and the material becomes

polarized. This means that the polarization does not disappear at high temperatures like in the displacive case, but average out instead, resulting in no total macroscopic polarization. [13]

2.3.1 Morphotropic Phase Boundary

The most common type of phase transitions change as a function of temperature or pressure. They are called polymorphic phase transitions and one example is the transition from paraelectric to ferroelectric. Another important phase transition for ferroelectrics is the morphotropic phase transition. This is when a transition changes as a function of composition while other variables are constant. The boundary between the phases in a morphotropic transition is called a morphotropic phase boundary (MPB) and is found as a mostly vertical line in the binary phase diagram. For ferroelectric materials, the term is often used to specifically describe the important phase transition between orthorombic and tetragonal phases. Perovskite solid solutions with a composition close to the MPB have been shown to exhibit a substantial increase in the dielectric permittivity. This leads to enhancement of properties like piezoelectric coefficient. [14] Furthermore, a straight MPB is important to ensure a temperature independent material.

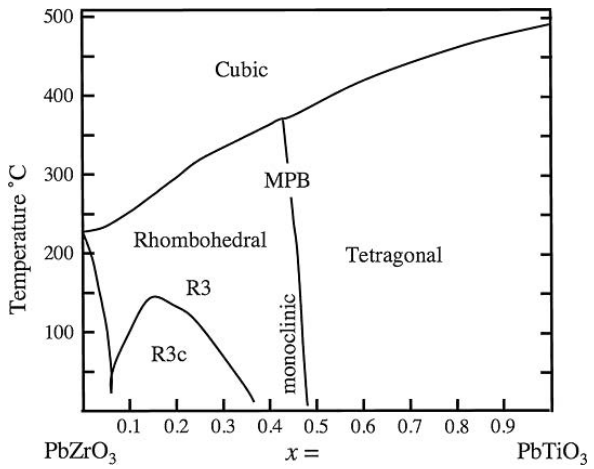

Figure 2.4: Phase diagram of lead zirconia titanate. Figure as reported by Jaffe *et al.* [15]

A classical solid solution is that of lead zirconia titanate (PZT). The end members of PZT is $PbZrO_3$ and $PbTiO_3$. At a mixture of around $0.48PbTiO_3$, there is a morphotropic phase transition between a rhombohedral and tetragonal phase. The phase diagram for PZT has been reported by Jaffe *et al.* and is shown in figure 2.4.[15] It is proposed that the crystal structures become degenerate at the phase transition, causing polarization rotation of the grains. This induces a stress that enhances the dielectric properties.[16,17,18]

2.4 Normal and Relaxor Ferroelectrics

When regarding dielectric response, there are two different types of ferroelectrics. The normal ferroelectrics in general follow the Curie-Weiss law, predicting an anomaly in dielectric susceptibility and high permittivity at the critical temperature as described in section 2.2.3.

The other type is relaxor ferroelectrics. In comparison to the normal ferroelectrics, the relaxor type materials have a broad and frequency-dependent critical temperature. In general, the dielectric permittivity decreases with increasing frequency and the critical temperature is shifted to higher temperatures. Relaxor ferroelectrics become anisotropic and gain a macroscopic polarization at temperatures significantly below the critical temperature.[19] It is well known that relaxor materials are generally highly inhomogeneous and it is often connected to some inherent disorder in the material. It has been proposed that the broad critical temperature is caused by different orientation in small regions called polar nanoregions. These nanoregions have different chemical composition and thus different dielectric polarization, causing a broadening of the dielectric permittivity.[19] Good examples of chemically disordered relaxor ferroelectrics include $PbMg_{1/3}Nb_{2/3}O_3$ (PMN)[19] and the solid solution $Ba(Ti_{1-x}Zr_x)O_3$ (BZT).[20] The relaxor properties have also been proposed to occur in systems with a mix of ferroelectric and antiferroelectric materials.[21]

One way to quantify and assign the type of ferroelectric was suggested by Uchino *et al.*, who proposed that plotting the reciprocal dielectric permittivity, $\frac{1}{\epsilon} - \frac{1}{\epsilon_m}$, against temperature, $T - T_m$, would result in a straight line following equation 2.5, where C' is a Curie-like constant and γ a critical exponent.[22] Producing a linear fit to the plotted results will give

a critical exponent close to 1 for normal ferroelectric materials, while relaxor like ferroelectrics will have a value closer to 2. In their work, Uchino *et al.* show that this is the case for the two normal ferroelectrics $BaTiO_3$ (BTO) and $KTaNbO_3$(KTN), and the relaxor type ferroelectrics $P(Mg_{1/3}Nb_{2/3})O_3$ (PMN) and $P(Zn_{1/3}Nb_{2/3})O_3$ (PZN).

$$\frac{1}{\epsilon} - \frac{1}{\epsilon_m} = (C')^{-1}(T - T_{\mathrm{m}})^{\gamma} \tag{2.5}$$

Multiple theories about relaxor ferroelectrics have been developed with different methods of parametrizing the relaxation. Another example is Vogel-Fulcher, which also applies different frequency measurements. Still, a good description of the microscopic effect of relaxor ferroelectrics is lacking.[23]

2.5 Tetragonal Tungsten Bronzes

The tetragonal tungsten bronze (TTB) is a crystal system first discovered and described in 1949 by Magnéli.[2] Because it is a relatively new structure, a rigorous theory has not yet been developed. It is an intricate system with a wide variety of possible material compositions. The general formula is $(A2)_4(A1)_2(C)_4(B1)_2(B2)_8O_{30}$. This allows for a large room of freedom in chemical substitution and testing with different elements to alter the structure and its functional properties. The two B sites form corner sharing octahedra with the oxygen atoms, resulting in BO_6 layers. These layers accommodate 3 different interstitial sites shaped as different polyhedra. The largest is the pentagonal A2 site, while the smaller A1 site is square. The latter can be referred to as the perovskite site because of how it and the four adjoining BO_6 form a shape similar to the perovskite structure. The C site is trigonal and the smallest site, therefore it is only able to be filled by small cations like Li. A TTB structure with atoms in all the sites is called stuffed, while filled TTBs have cations in all A sites and holes in the C sites.[3] Unfilled variants also exist, which lack some atoms in the A sites and often exhibit disorder and relaxor properties. One example of unfilled TTBs is $Sr_xBa_{1-x}Nb_2O_6$, which depending on the composition either is a normal or relaxor ferroelectric.[24] Additional ways of introducing disorder is by substituting atoms with different valencies. It is for instance possible to substitute Nb^{5+} with La^{4+} or even O^{2-} with

F^-.[25] A figure of the TTB structure displayed looking down the c axis is shown in figure 2.5.

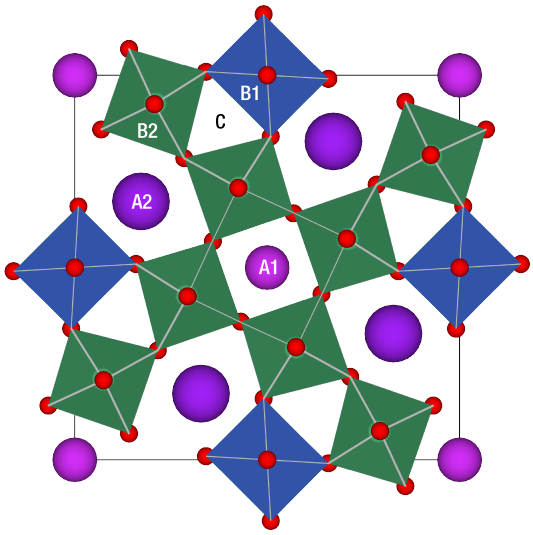

Figure 2.5: Prototype tetragonal tungsten bronze structure looking down the c axis. The different atomic sites are labeled corresponding to the general formula $(A2)_4(A1)_2(C)_4(B1)_2(B2)_8O_{30}$.

The TTB structure is often compared to the better known and well researched perovskite structure, as it is a simpler and better known crystal system. Attempts at transferring theory to the TTBs have been performed, for example the geometric tolerance-factor defined by Goldschmidt for the perovskites in 1926.[26] The tolerance factor uses the ionic radius of the atoms in the structure to determine which structure it adopts. It can also say something about whether or not the structure is likely to be ferroelectric. From this theory, Wakyia *et al.* suggested separate tolerance factors for each A site in the TTB system.[27] The tolerance factor for the A1 site, t_{A1}, is given in equation 2.6. It is the same as for the perovskites, as the shape is identical. In comparison, the A2 sites have a different geometric shape and coordination and the tolerance factor, t_{A2}, is reliant upon the distance to three different neighbouring oxygen atoms. The formula for calculating the A2 tolerance factor is given in equation 2.7. In both equa-

tions, R denotes the atomic radius and the subscript denotes either the occupied site or atom. There are twice the number of A2 sites compared to A1 sites, so the A2 sites must be counted twice in the total tolerance factor given in equation 2.8. One use of the TTBs total tolerance factor is to identify whether the structure is a normal or relaxor ferroelectric.[3]

$$t_{A1} = \frac{(R_{A1} + R_O)}{\sqrt{2}(R_B + R_O)} \tag{2.6}$$

$$t_{A2} = \frac{(R_{A2} + R_O)}{\sqrt{23 - 12\sqrt{3}}(R_B + R_O)} \tag{2.7}$$

$$t_{TTB} = \frac{(t_{A1} + 2t_{A2})}{3} \tag{2.8}$$

The prototype structure for TTBs is the tetragonal P4/mbm structure. In a transition to an orthorombic unit cell, the unit cell can be rotated by 45°, causing an increase of the lattice parameters with a factor of $\sqrt{2}$. Therefore, to compare the lattice parameters of an orthorombic unit cell to a tetragonal, they might need to be scaled by this factor.

2.6 Barium Sodium Niobate

Barium Sodium Niobate (BNN) is a filled tetragonal tungsten bronze with the general structure $Ba_4Na_2Nb_{10}O_{30}$. It was first synthesised and investigated in 1967 by researchers at the Bell Telephone Laboratories.[28] They investigated many different TTBs as potential replacements for non-linear materials. This was because many TTBs were reported to not suffer from optical damage at room temperature, which other non-linear materials used at the time, like $LiNbO_3$, usually did. Among these, BNN was found to be the most promising for use as an optical harmonic generator and optical parametric oscillator. Compared to $LiNbO_3$, BNN has a more reproducible phase match temperature with a deviation of 10 °C from crystal to crystal. They found the melting point to be around 1500 °C, although later studies have reported slightly lower melting temperatures around 1440 °C.[29] The ferroelectric transition has a high critical temperature at 560 °C, resulting in polarization in the c axis. Around 300 °C there is a

ferroelastic transformation accompanied by microtwinning and a change from the tetragonal 4mm to the orthorombic mm2 point group.

Some later studies have focused on determining the ferroelectric structure of BNN. Currently, the room temperature structure that can be found in the International Centre for Diffraction Data is the orthorombic space group Pba2. The lattice parameters have been reported to be $a = 12.425\,\text{Å}$, $b = 12.484\,\text{Å}$ and $c = 3.977\,\text{Å}$. This is referencing the work of Tomaszewski from 1992 [30] and Foulon *et al.* from 1996. [31] A paper from 2001 [32] reviewed the earliest structural determination of BNN made by Jamieson *et al.* in 1969. [33] Jamieson *et al.* determined that the paraelectric structure takes on the tetragonal 4/mmm structure and the ferroelectric structure is tetragonal 4mm. Below the ferroelastic transition at 260 °C, the structure takes on the orthorombic Cmm2 space group with lattice parameters $a = 17.591\,82\,\text{Å}$, $b = 17.625\,60\,\text{Å}$ and $c = 3.994\,915\,\text{Å}$. Additionally, Jamieson *et al.* recorded a low temperature transition at −160 °C back to the tetragonal 4mm structure. The room temperature structure was thus challenged by Foulon *et al.*, who could not achieve a good fit with the Cmm2 space group to their samples. They found the intensities to fit better with the tetragonal P4bm. In addition, they argued that this simplifies the ferroelastic transition, as it is not required to scale the lattice parameters like Jamieson *et al.* did. A recently published paper by Aamlid *et al.* challenges Foulon *et al.* and indicates that Jamieson *et al.* was correct. Based on XRD data and DFT analysis, they argue that the Cmm2 structure better explains the splitting of certain peaks and that the intensity can be explained by cationic disorder. [6]

The density of BNN is reported to be somewhere between $5.36\,\text{g}\,\text{cm}^{-3}$ and $5.4\,\text{g}\,\text{cm}^{-3}$. [29,30,33,34] The measurements were performed using both hydrostatic measurements on single crystal samples and calculated theoretically from x-ray diffraction data. Different samples of BNN have been reported with a difference in theoretical density, which has been attributed to non-stoichiometry. [33,35] The structure is usually documented to have more barium and less sodium, and this can vary slightly depending on the processing parameters. The excess barium is occupying some of the A1 sites. [6] Even though BNN is mostly reported as a conventional ferroelectric with a sharp anomaly in the dielectric permittivity, it can be doped with fluorine to exhibit more relaxor-like ferroelectric properties with a

below room temperature transition.[25]

2.7 Potassium Bismuth Niobate

Potassium Bismuth Niobate (KBiN) is a filled tetragonal tungsten bronze with the general structure $K_4Bi_2Nb_{10}O_{30}$. It was made independently at the same time by Ismailzade in 1963[36] and Krainik *et al.* in 1964.[37] These studies greatly disagreed on the critical temperature. Ismailzade found the critical temperature to be 350 °C, while Krainik found it to be 160 °C. Later studies show that the critical temperature generally is located around 360-400 °C and indicates that it is dependent on the chemical composition.[38,39,40] Sugai and Wada reinvestigated the KBiN system and found the crystals to have the tetragonal tungsten bronze structure with $a = b = 17.85\,\text{Å}$ and $c = 7.84\,\text{Å}$ and a theoretical density of $5.29\,\text{g}\,\text{cm}^{-3}$. KBiN is often reported to have the same pseudo-tetragonal crystal structure as BNN, with the polar axis along the c axis.[39,41] This is disputable, as both computational work and HTXRD recorded by the author indicates that the polarization is in the ab plane.[1,42] Because of conflicting results, the space group has not yet been properly determined.

3 Experimental Setup

3.1 Synthesis

Six different compositions were prepared: the end members of the solid solution, KBiN and BNN, as well as four samples with varying composition evenly spaced between the two end members. The samples have been named after the content of KBiN and are referred to as 0.8KBiN, 0.6KBiN, 0.4KBiN and 0.2KBiN.

The powders were prepared from scientific grade precursors and information on purity and supplier is given in table 3.1. Precursors were mixed in a stoichiometric ratio for the given sample and mixed with ethanol in a mortar. This was to minimize loss of powder from it sticking to the weighing boat and from becoming airborne. After mixing, the wet solution was allowed to dry in a fume hood overnight. A subsequent grinding was performed after the overnight drying to ensure a homogeneous mixture. Approximately 10 g was made of each composition.

Table 3.1: A list of precursors used, their respective purity and producer.

Precursor	Purity [%]	Producer
$BaCO_3$	99.98	Sigma Aldrich
Na_2CO_3	99.0	Sigma Aldrich
Bi_2O_3	99.9	Sigma Aldrich
K_2CO_3	99.0	Merck
Nb_2O_5	99.9	Sigma Aldrich

3.2 Powder Treatment and Shaping

Before calcination, powder was shaped into large pellets by uniaxial pressing at a force of 2 t. After calcination, the powder was ball milled in an ethanol slurry for 24 hours on a high speed ball mill from US stoneware, using YTZ balls as milling media. Ethanol was used because pH paper tests indicated that water can dissolve cations from the powder. After milling, the slurry was dried under vacuum and shaped into short cylindrical samples with a combination of uniaxial pressing at 4 kN and subsequent compaction using a CIP set at 2 kbar.

3.3 Heat Treatment

Heating and cooling of all the samples during calcination and sintering was done at a rate of $200\,\mathrm{K\,min^{-1}}$. The general hold time and hold temperature utilized for calcination and sintering of the different compositions are listed in table 3.2 and 3.3, respectively. It is explicitly explained in section 4 if a sample went through a different heat treatment. The sintered samples were encased in a cloak of sacrificial powder with the same composition to reduce evaporation of volatile species. To measure evaporation, the powder used for pressing the pellets was weighed and compared to the weight of the finished pellet.

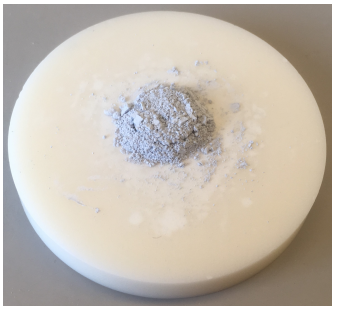

Figure 3.1: Sample encased in sacrificial powder on an alumina plate ready for sintering.

3.4 X-Ray Diffraction

Multiple different XRD instruments were used for measurements, primarily a Bruker D8 Focus and a Bruker D8 A25 DaVinci X-ray Diffractometer, both equipped with a copper K-α x-ray source without monochromator and LynxEye^{TM} SuperSpeed Detectors. Samples were prepared in silicon cavity holders. All measurements were taken in one hour in the angle range 5-75 2θ with a stepsize of 0.013.

Table 3.2: Tabulated values for the calcination parameters used for the different compositions.

Sample	Hold temperature [°C]	Hold time [hours]
BNN	900	2
0.2KBiN	880	2
0.4KBiN	860	2
0.6KBiN	840	2
0.8KBiN	820	2
KBiN	800	2

Table 3.3: Tabulated values for the sintering parameters used for the different compositions.

Sample	Hold temperature [°C]	Hold time [hours]
BNN	1260	1
0.2KBiN	1240	1
0.4KBiN	1220	1
0.6KBiN	1200	1
0.8KBiN	1180	1
KBiN	1150	1

3.5 Scanning electron microscope

The microstructure of the samples was investigated using scanning electron microscopy (SEM). The samples were first fractured using a metal pellet crusher and coated in a thin layer of gold using a gold sputter, to make the sample surface conductive. A Hitachi S-3400N was used to take the SEM images.

3.6 Impedance Spectroscopy

For dielectric spectroscopy, a ProboStat^{TM} from NOREC was used in a setup designed for impedance spectroscopy. The samples were first surface treated by sanding and cleaning with ethanol in an ultrasonic cleaner to make the surfaces flat and parallel. Platinum electrodes were applied as a layer of platinum paste, which was dried for 15 minutes at 125 °C. This process was repeated for the opposite side. Afterwards, the electrodes were cured in place at 800 °C for 15 minutes. Samples were heated from room temperature at a constant rate of $2\,\mathrm{K\,min^{-1}}$ up to 600 °C for 0.6KBiN, 0.8KBiN and KBiN, while BNN, 0.2KBiN and 0.4KBiN were heated to 700 °C. The reason for using a higher temperature for the BNN rich samples is the higher critical temperature for BNN. Probing voltage was set to $1\,\mathrm{V\,mm^{-1}}$ and was dependent on the sample thickness. Samples varied in thickness, but were all in the range of 1-3 mm. The measurements were taken continuously with a varying frequency ranging from 1 to 10×10^6 Hz. Samples were heated and cooled twice.

3.7 Density Measurements

Green density was measured geometrically using calipers and the assumption that the samples are made as perfect cylinders. This measurement was used to judge how well the samples had been shaped before sintering. Archimedes' method was used to measure the density of sintered samples more accurately. The theoretical density of solid solutions was calculated as a linear approximation between the end members.

4 Results

4.1 Density and Microstructure of Samples

All the samples experienced some weight loss after sintering, roughly between 2 % and 5 % for all samples. The difference between samples of BNN is plotted in figure 4.1. The weight loss increased slightly with increasing sintering temperature. The density also increased significantly. An overview of the density and weight loss of all the different compositions is found in table 4.1. Compositions on the BNN rich side have a higher sintering temperature and also a higher variety with regards to both density and weight loss.

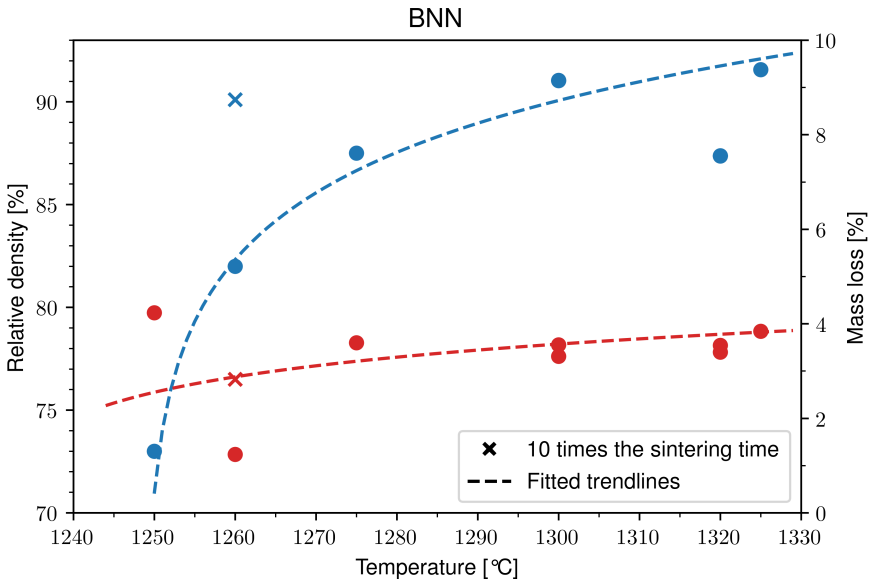

Figure 4.1: Comparison of relative density and weight loss for BNN samples as a function of sintering temperature. Polynomial fits are used to highlight the trend and are excluding outliers in the data.

Table 4.1: Weight loss and density for all the different compositions.

Composition	Sintering temp. [°C]	Number of samples	Relative density [%]	Weight loss [%]
BNN	1260	2	86.0 ± 4.0	2.0 ± 0.8
0.2KBiN	1240	3	87.0 ± 3.2	6.7 ± 0.4
0.4KBiN	1220	3	90.4 ± 1.3	7.7 ± 1.2
0.6KBiN	1200	3	96.5 ± 1.1	4.1 ± 0.2
0.8KBiN	1180	2	91.6 ± 1.8	4.4 ± 0.4
KBiN	1150	3	97.4 ± 0.3	0.7 ± 0.1

Microstructure of BNN

Figure 4.2 shows a BNN sample made during the author's project work in 2019.[1] It has millimetre large grains that are visible to the naked eye. New BNN samples were made from a new powder batch. All the samples were processed in the same general process, except varying the sintering temperature. All the samples had similar green density above 50 %. A comparison of SEM images of the fracture surface of samples sintered at 1250 °C, 1260 °C, 1275 °C and 1300 °C is shown in figure 4.4. BNN sintered at and below 1260 °C have grains that are smaller than 5 µm. At 1275 °C, large grains around 50 µm with large pores inside the grains have formed. There are also smaller grains scattered between the large grains. The same is true for the sample sintered at 1300 °C, where mostly large grains are visible in the fracture, but small grains are clearly visible on the thermally etched surface of the pellet, as shown in figure 4.3.

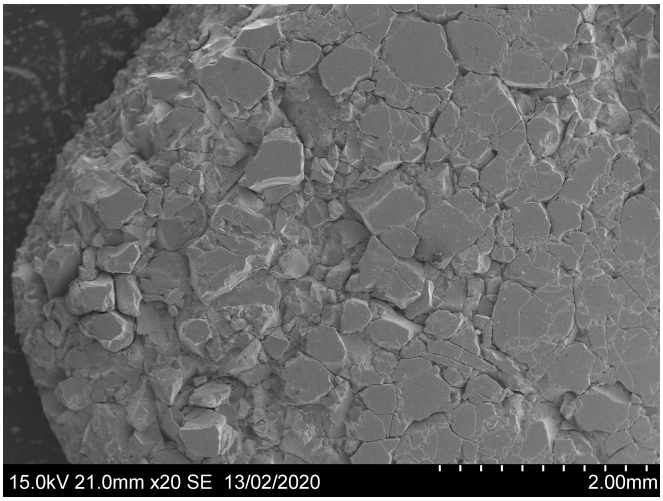

Figure 4.2: Low magnification SEM image of the surface of BNN sample, made in previous work, sintered for 2 hours at 1325 °C. [1]

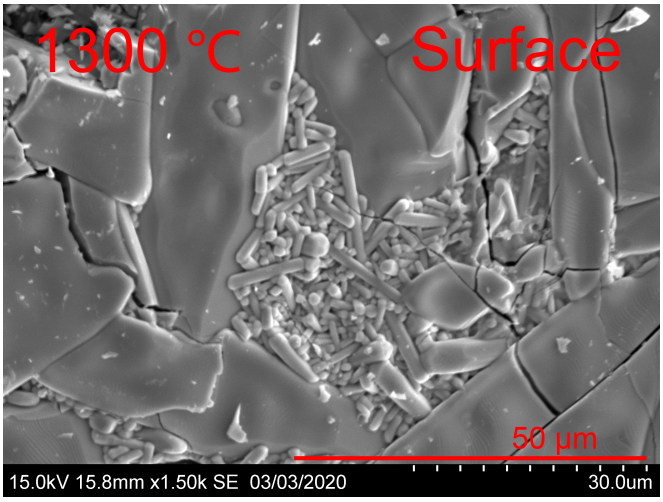

Figure 4.3: Surface of BNN pellet sintered for 1 hour at 1300 °C.

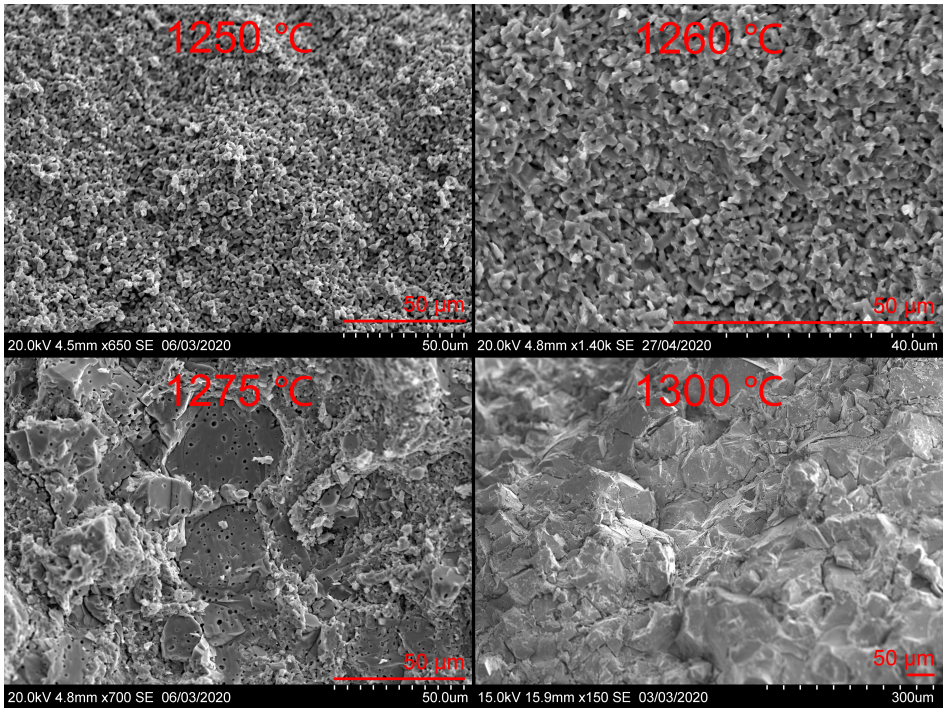

Figure 4.4: Comparison of the microstructure of BNN samples sintered for 1 hour at different temperatures ranging from 1250 °C to 1300 °C. Note the different magnification of the images. The red bar is 50 µm for all images.

Microstructure of All Samples

A comparison of the SEM images of all samples was made to investigate how the microstructure with grains and pores of the samples might differ from each other. In figure 4.5, a comparison of the fracture planes of all sample compositions is shown. The images have not been taken perpendicular to the fracture plane and a zoomed in image is available in appendix A. Note that the image of BNN is zoomed in more than the others.

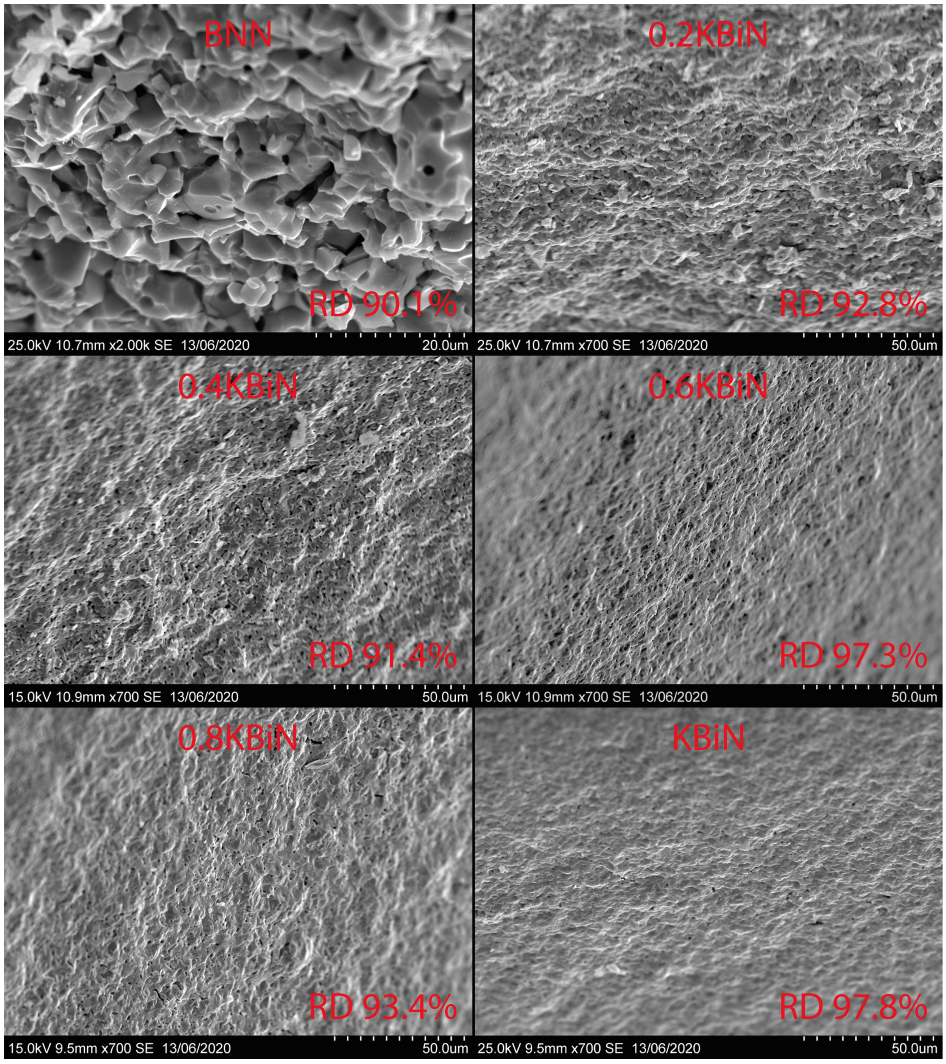

Figure 4.5: SEM images of the microstructure of all samples. RD denotes the relative density. Notice that images have not been taken perpendicular to the fracture plane and that BNN is zoomed in more than the others.

4.2 X-ray Diffraction

Attempts were made to autoindex the x-ray diffraction (XRD) pattern of KBiN with respect to other space groups than those previously reported. This was attempted because the HTXRD data collected for the project work showed some small peaks that disappeared after heating above 400 °C, which reappeared upon cooling. [1] This indicated that KBiN has a different crystal structure at room temperature, which has not been reported before. The attempts made did not give any results and the space group and crystal structure of KBiN is still unknown.

X-ray diffractograms of all sintered compositions were compared and plotted in figure 4.6. All XRDs have characteristic peaks corresponding to the aristotype TTB structure P4/mbm.

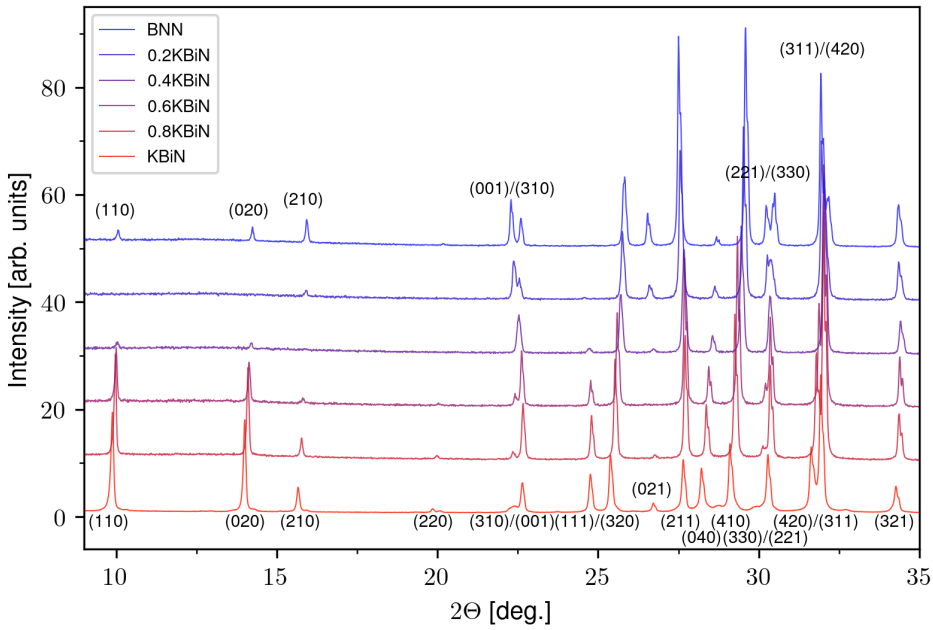

Figure 4.6: X-ray diffraction of the different compositions after sintering. Miller indicies are given for the aristotype tetragonal tungsten bronze structure, P4/mbm.

A small subset of the diffractogram of all compositions from 29-31 2θ is shown in figure 4.7. From the XRD diffractogram, the peak after 30 2θ shows clear orthorombic splitting in BNN, which disappears with increasing solid solution of KBiN. Because of this, the tetragonal P4bm structure was used for Pawley refinement of KBiN rich samples, while BNN's room temperature space group Cmm2 was used for the BNN rich side.

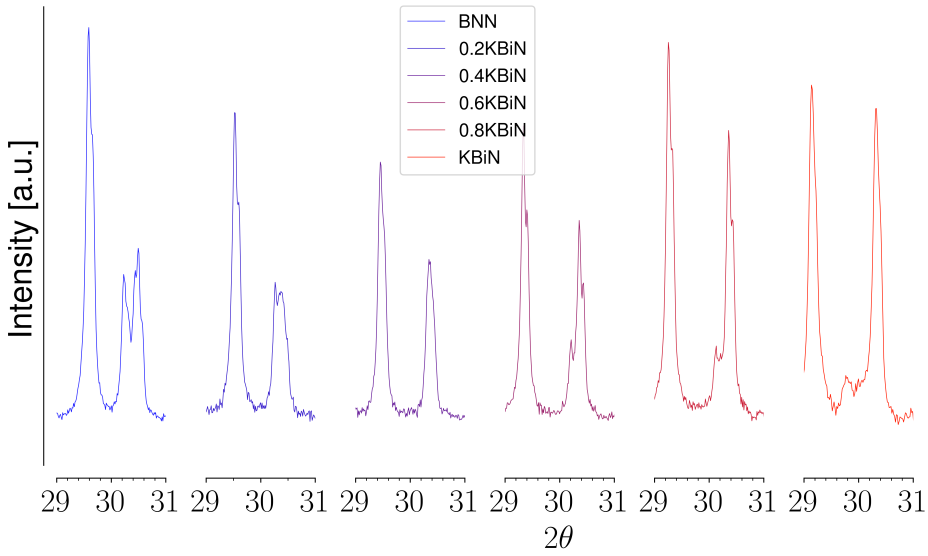

Figure 4.7: Comparison of peaks at 29-30 2θ for the different compositions.

4.2.1 Pawley Refinement

A zoomed in view of peaks in the ranges 10-16 2θ, 22-26 2θ and 30-33 2θ are given in appendix B.

Orthorombic (Cmm2)

Pawley refinement of the BNN rich side of the solid solution was done using the Cmm2 space group with the starting parameters 17.6 Å for a and b parameters and 3.9 Å for the c parameter.

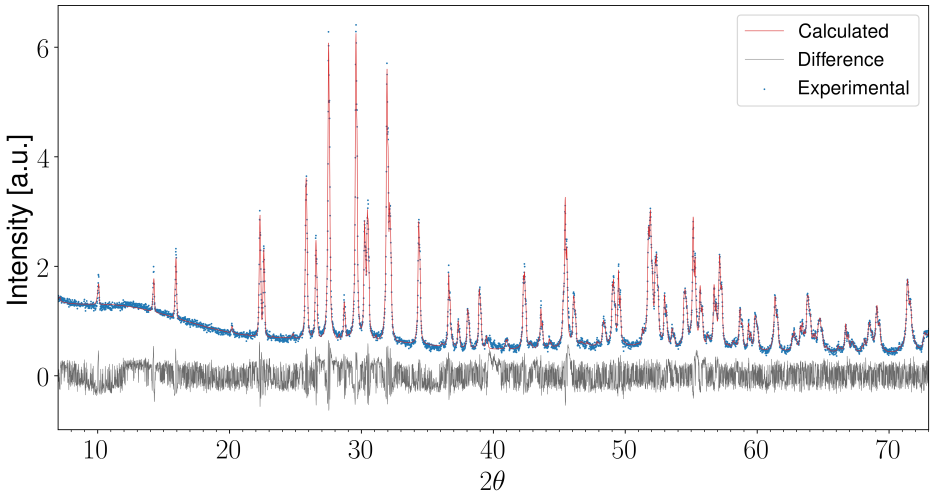

Figure 4.8: Pawley refinement of BNN diffractogram using the Cmm2 structure. $R_{wp} = 9.61$ and $R_{exp} = 3.76$.

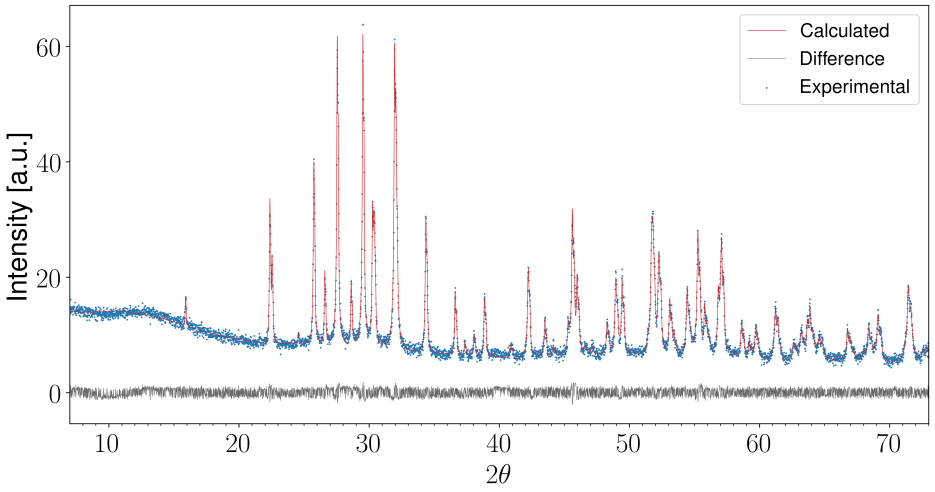

Figure 4.9: Pawley refinement of 0.2KBiN diffractogram using the Cmm2 structure. $R_{wp} = 10.24$ and $R_{exp} = 8.11$.

Tetragonal (P4bm)

Pawley refinement of the KBiN rich side of the solid solution was done using the P4bm space group with the starting parameters 12.6 Å for the a parameter and 3.9 Å for the c parameter.

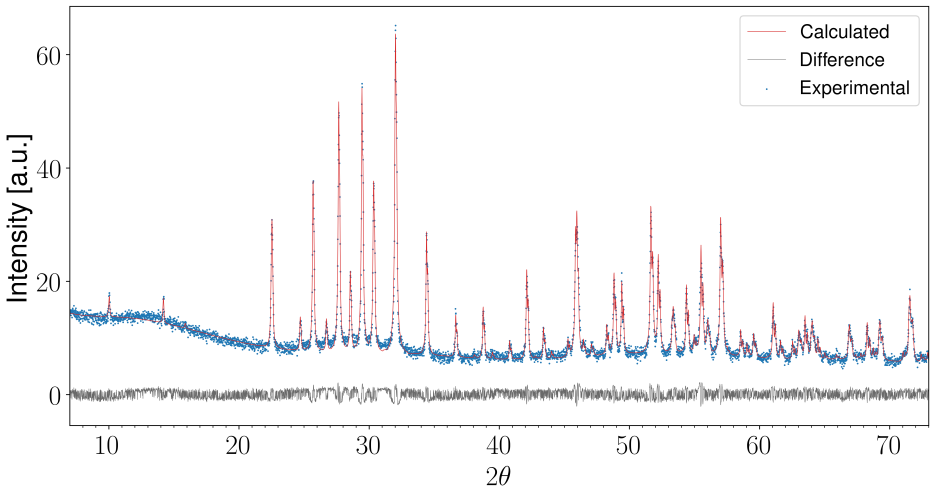

Figure 4.10: Pawley refinement of 0.4KBiN diffractogram using the P4bm structure. $R_{wp} = 13.71$ and $R_{exp} = 8.58$.

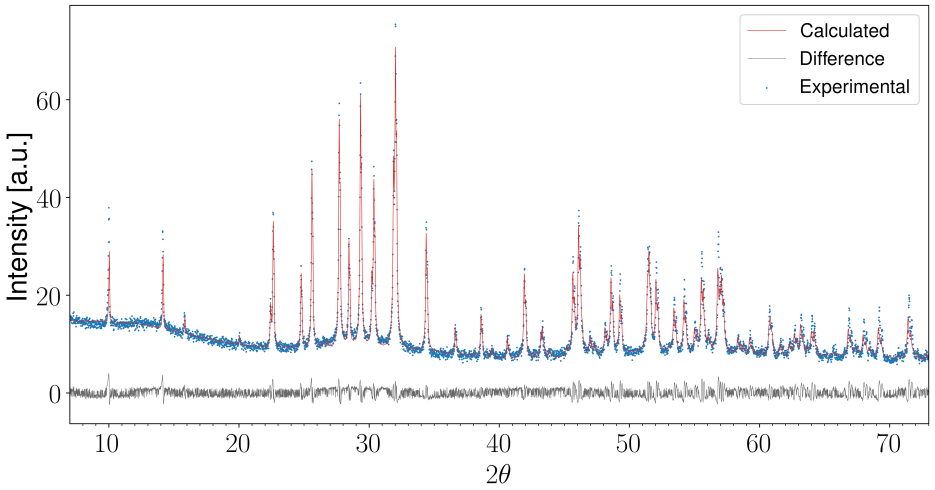

Figure 4.11: Pawley refinement of 0.6KBiN diffractogram using the P4bm structure. $R_{wp} = 20.25$ and $R_{exp} = 7.56$.

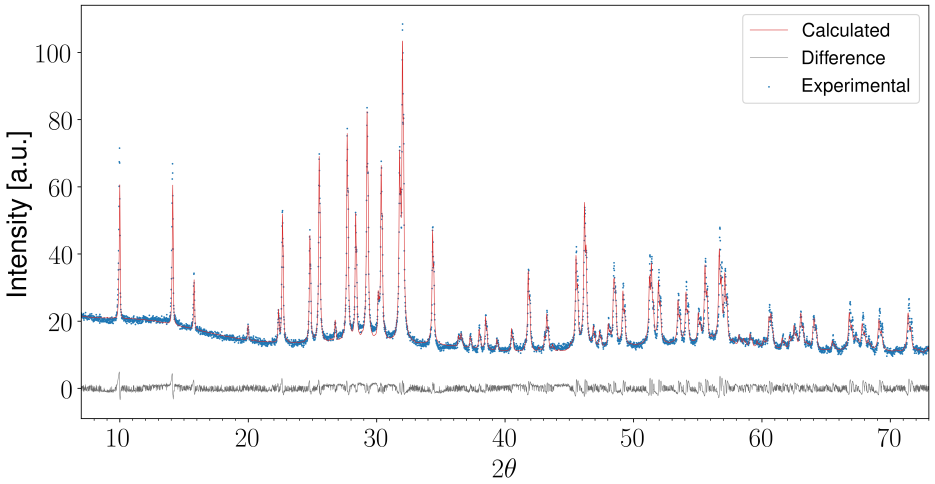

Figure 4.12: Pawley refinement of 0.8KBiN diffractogram using the P4bm structure. $R_{wp} = 16.14$ and $R_{exp} = 5.03$.

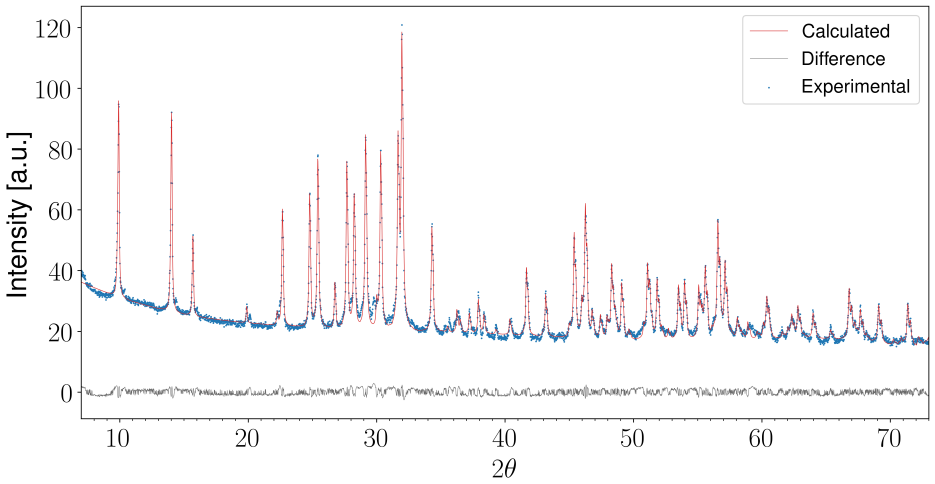

Figure 4.13: Pawley refinement of KBiN diffractogram using the P4bm structure. $R_{wp} = 8.89$ and $R_{exp} = 3.56$.

4.2.2 Evolution of the Lattice Parameters

The lattice parameters obtained through Pawley refinement of the different compositions was plotted in figure 4.14. The orthorombic lattice parameters have been scaled by $\sqrt{2}$ to be comparable with the tetragonal parameters. The c parameter decreases, while the a and b parameters increase with increasing content of KBiN in the solid solution. The a and b parameters increase steadily until they cross right before 0.4KBiN. The value for the c parameter significantly drops at the same point. There is a non-linear change in the a parameter between 0.4KBiN and 0.6KBiN.

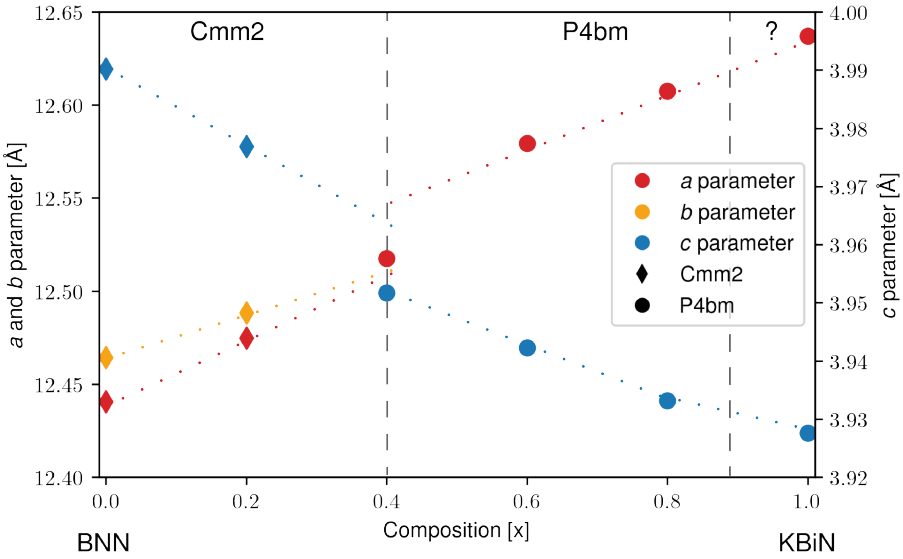

Figure 4.14: Evolution of the lattice parameters as a function of composition. Orthorombic Cmm2 scaled by $\sqrt{2}$ was used for the BNN rich side and the tetragonal P4bm was used for the KBiN rich side.

4.3 Dielectric Measurements

4.3.1 Critical Temperature

Prior dielectric studies performed on BNN and KBiN correspond well with the dielectric measurements.[6,28,38] The exact critical temperature varies slightly between studies, likely due to small differences in composition. Measurements of all compositions with the critical temperature is given in figure 4.15. Only data from the first heating is shown at a frequency of 1 MHz.

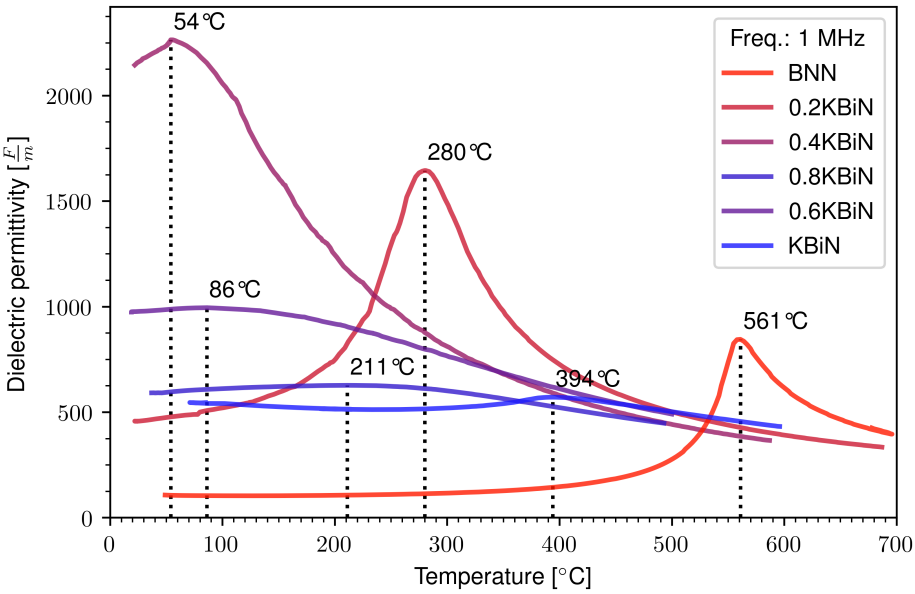

Figure 4.15: Dielectric measurements for all compositions, only showing the first heating at a frequency of 1 MHz. The vertical lines mark the critical temperature.

4.3.2 Thermal Hysteresis in BNN Rich Samples

There are a couple of differences in the dielectric measurements based on thermal hysteresis seen for the BNN rich samples. The biggest difference is for BNN, where the critical temperature changes position slightly, as seen in figure 4.16. This is not seen for any of the other samples. For BNN, 0.2KBiN and 0.4KBiN, the dielectric permittivity is higher for cooling than heating. This can also be seen in the dielectric loss, plotted as $\tan\delta$. Lower frequency measurements at 1 kHz show that there is a difference between the first and second run, as can be seen in figure 4.17. On the first run the dielectric permittivity increases, but it stabilizes for the second run.

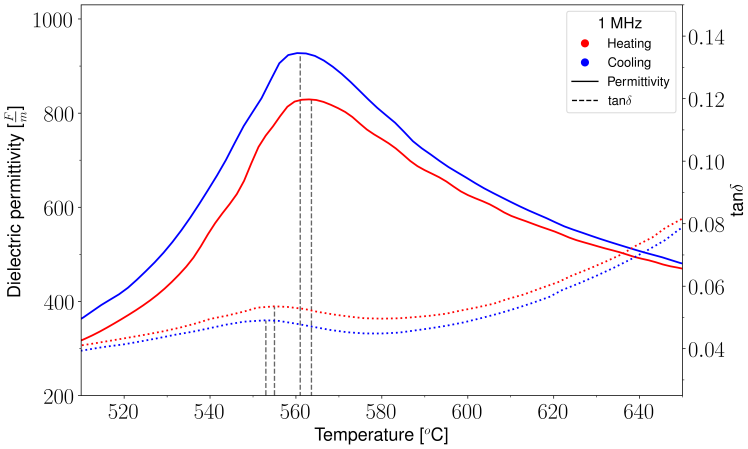

Figure 4.16: Temperature dependence of dielectric properties of BNN measured at 1 MHz. The influence of thermal history is indicated by vertical lines marking the critical temperature.

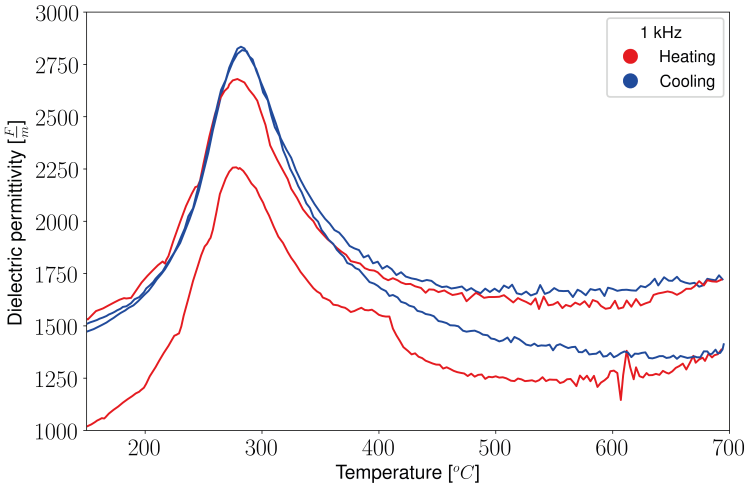

Figure 4.17: Temperature dependence of dielectric permittivity for 0.2KBiN measured at 1 kHz. The first heating cycle is the lowest line.

4.3.3 Frequency Dispersion and Dielectric Loss

Most of the samples show significant frequency dispersion accompanied by a significant increase in dielectric loss at lower frequencies. The measurements for the dielectric permittivity over a frequency range of 10^3-10^6Hz are given in figure 4.18 for BNN rich samples and 4.19 for KBiN rich samples. For clarity, only the measurements from the first heating is shown.

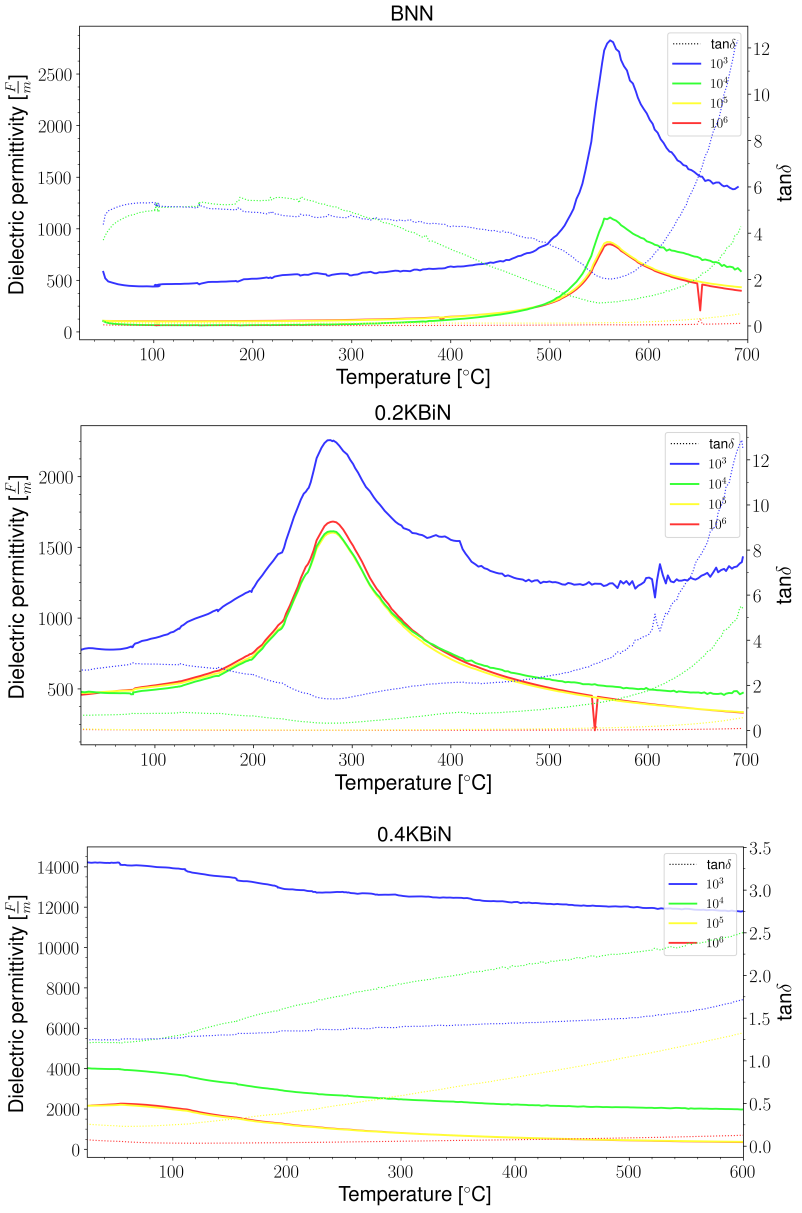

Figure 4.18: Frequency dependence of the dielectric permittivity and dielectric loss in BNN, 0.2KBiN and 0.4KBiN.

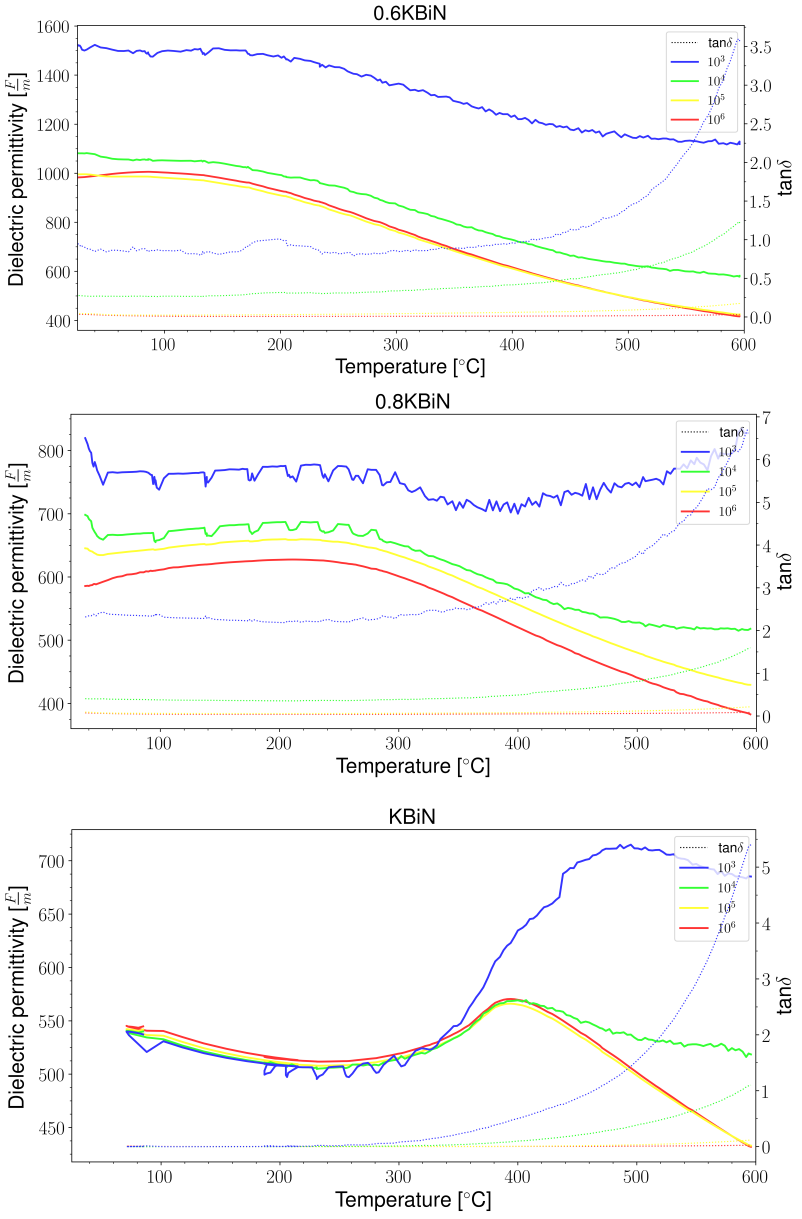

Figure 4.19: Frequency dependence of the dielectric permittivity and dielectric loss in 0.6KBiN, 0.8KBiN and KBiN.

4.4 Phase Diagram

When plotting the peak dielectric permittivity against composition in figure 4.20, it is clear that the highest value is achieved for 0.4KBiN. Note that the blue markers show the permittivity at the critical temperature and the red markers show the value at room temperature. This difference is important because the highest dielectric permittivity is located at the critical temperature, which decreases with increasing solid solution.

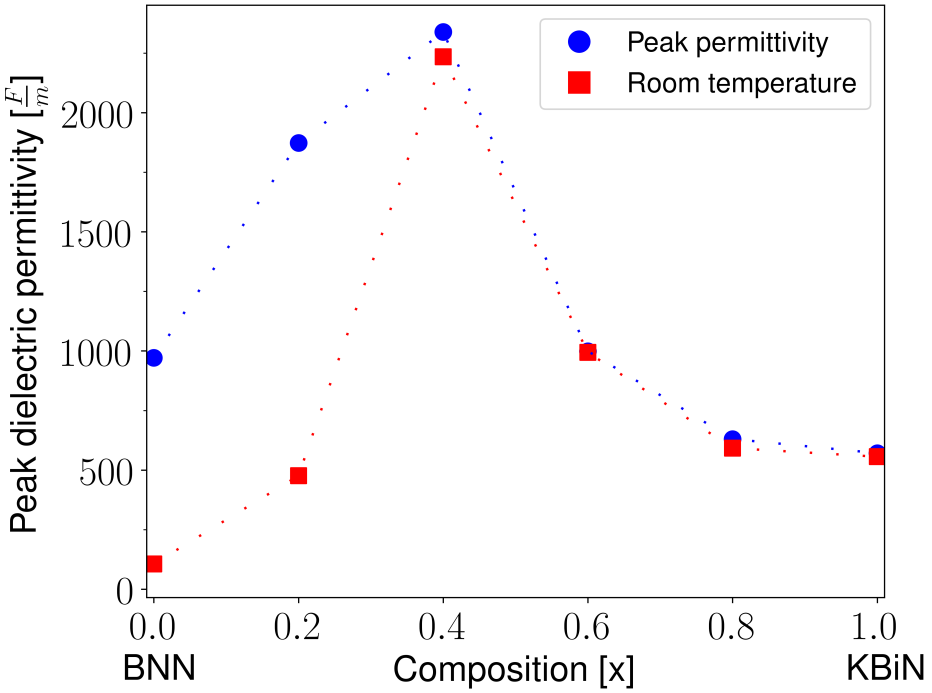

Figure 4.20: Room temperature and peak dielectric permittivity as a function of composition.

Using the information from the x-ray diffraction and the dielectric data, a phase diagram has been drawn in figure 4.21. The points indicate the critical temperatures of the composition where there is a polymorphic phase transition to the paraelectric P4/mbm phase. The different phases for BNN are marked on the left side and the unknown structure for KBiN at the right side. The straight vertical line at 0.4KBiN indicates the location of a MPB between the orthorombic Cmm2 phase and the tetragonal Pba2 phase.

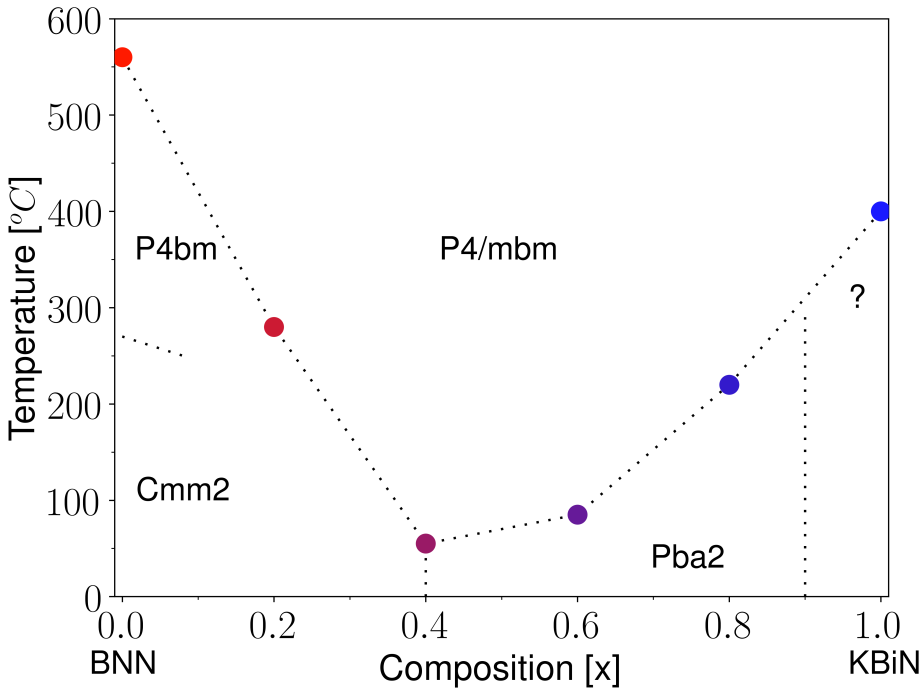

Figure 4.21: Phase diagram of the solid solution of BNN and KBiN.

5 Discussion

5.1 Morphotropic Phase Boundary

According to Vegard's law, the lattice parameters change continously between two phases with similar crystal structure.[43] It is known that the end members, KBiN and BNN, have different crystal structures, therefore a change in the evolution of the lattice parameters is expected. As seen in figure 4.14, the lattice parameters evolve continuously up to the 0.4KBiN solid solution. Here, there is a jump in the value of both the a and c lattice parameters. The change in the c parameter occurs on the BNN rich side, while the change in the a parameter occurs on the KBiN rich side. This indicates that there are two distinct phases existing in the solid solution in this region: one phase for the KBiN rich side and another for the BNN rich side, separated at the 0.4KBiN composition. The change in lattice parameters show that the polarization is moving from the c axis in BNN to the ab plane with increasing solid solution. From the x-ray diffractograms shown in figure 4.7, a characteristic orthorombic splitting of the peak around 30 2θ is clearly visible for BNN and 0.2KBiN. This splitting is also shown by Aamlid *et al.* in their study of BNN.[6] For 0.6KBiN and 0.8KBiN, this peak resembles a tetragonal splitting. It is harder to tell for 0.4KBiN, but considering that the a and b lattice parameters approach the same value, it is thought to adopt a tetragonal structure. This strongly indicates that there is a morphotropic phase transition around this composition.

From the dielectric data in figure 4.20, it is clear that 0.4KBiN has a higher dielectric permittivity compared to the other compositions, both at room temperature and at their respective critical temperatures. A higher dielectric permittivity is expected at the morphotropic phase boundary, due to the existence of different polarization modes.[16] Based on the x-ray diffractograms and the dielectric data, a proposed phase diagram was drawn and can be seen in figure 4.21. As seen, the critical temperature decreases with increasing solid solution and seems to do so towards a 0.5BNN-0.5KBiN composition.

5.2 Relaxor Properties

There is agreement that both BNN and KBiN behave as normal ferroelectrics.[3] They have distinct peaks in the dielectric permittivity at the critical temperature, which is independent of frequency variation. Among the solid solution compositions, 0.2KBiN and 0.4KBiN also have distinct peaks, although they are broader than the BNN peak. The 0.6KBiN and 0.8KBiN compositions have very broad peaks, which point towards relaxor behaviour. One would expect there to also be a frequency dependence of the critical temperature, which could be analysed using Vogel-Fulcher analysis. However, this is hard because of the broadness of the peaks and the fact that the data suffers from frequency dispersion and high dielectric loss, as can be seen in figure 4.18 and 4.19. The frequency independent method described by Uchino *et al.*[22] was applied instead. Figure 5.1 shows the reciprocal dielectric permittivity plotted against temperature for all the different compositions, as well as data from Uchino *et al.* for two well known normal ferroelectric materials and two relaxors. Values for the fitted variables C' and γ for the different compositions and data gathered from Uchino *et al.* are listed in table 5.1. This supports the view that the solid solution compositions exhibit some relaxor properties.

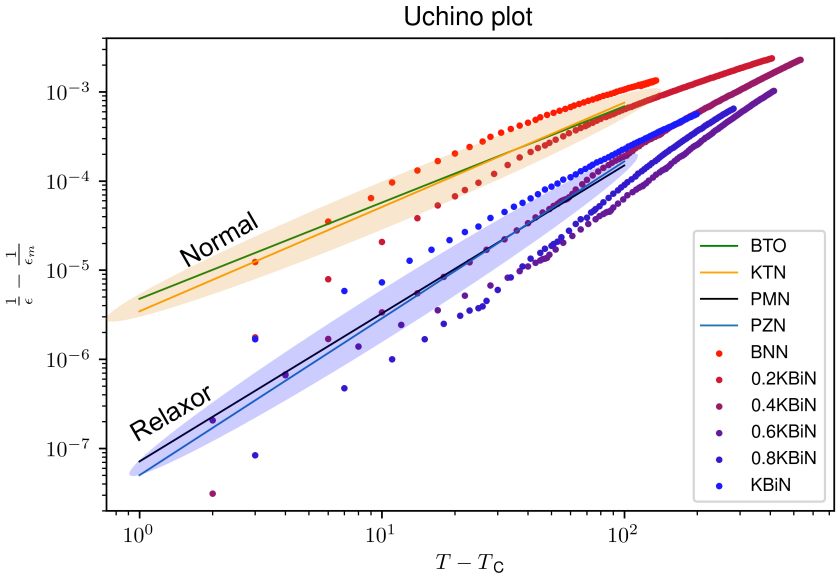

Figure 5.1: Logarithmic plot of the reciprocal permittivity against temperature for the different solid solutions prepared in this master thesis and data on the normal ferroelectrics $BaTiO_3$ (BTO), $KTaNbO_3$ (KTN) and the known relaxors $P(Mg_{1/3}Nb_{2/3})O_3$ (PMN) and $P(Zn_{1/3}Nb_{2/3})O_3$ (PZN) from Uchino *et al.* for comparison.[22]

Table 5.1: Tabulated values for the fitted critical exponent, γ, and the Curie-like constant, C', for the different compositions, as well as data on the normal ferroelectrics $BaTiO_3$ (BTO), $KTaNbO_3$ (KTN) and the known relaxors $P(Mg_{1/3}Nb_{2/3})O_3$ (PMN) and $P(Zn_{1/3}Nb_{2/3})O_3$ (PZN) from Uchino *et al.* for comparison.[22]

Composition	γ	C' (10^5)
KBiN	1.4	29
0.8KBiN	1.9	800
0.6KBiN	2.0	1350
0.4KBiN	1.6	89
0.2KBiN	1.3	9
BNN	1.1	2

	γ	C' (10^5)
BTO	1.08	2.1
KTN	1.17	2.9
PMN	1.64	140
PZN	1.76	200

Another aspect to consider is the crystal-chemical framework for TTB compounds proposed by Zhu *et al.*[3]. Their article describes how it is possible to group different TTBs with regards to a structure factor into normal or relaxor ferroelectrics. Calculating the structure factor for BNN and KBiN from the data they adopted from Shannon and Prewitt, the values lie close to the relaxor region.[44] It is possible that the increased disorder from a mixed composition induces relaxor properties in the system.

5.3 Thermal Hysteresis

The thermal hysteresis seen in figure 4.16 shows that BNN has a first order phase transition from the paraelectric to the ferroelectric phase. The thermal hysteresis is caused by the paraelectric phase being metastable, resulting in a critical temperature at a lower temperature compared to upon heating.[45] BNN has also been shown to have a first order transition by means of dilatometry.[6] In the other compositions, an offset of the critical temperature is not seen, indicating that the transitions for these are of second order.

Another thermal history effect lies in the difference in dielectric permittivity between heating and cooling. This is a sign of a form of relaxation in the system. It is seen as a peak in the permittivity only for lower frequency measurements in 0.2KBiN, as shown in figure 4.17. The peak is

only visible for the first heating at a temperature of 400 °C. After this, the permittivity stabilizes at a higher value and does not change upon heating again. The effect can be explained by oxidation that causes a relaxation, which can occur at these temperatures.

5.4 Microstructure and Composition

5.4.1 Abnormal Grain Growth in BNN

In the scanning electron microscope (SEM) image of BNN in figure 4.4, abnormal grain growth is seen for sintering temperatures at 1275 °C and above. It causes an undesirable microstructure that leads to weak mechanical strength and higher dielectric loss, due to pores in the material. The sample imaged has micro cracks, which probably occurred during the transition to the ferroelectric phase. At this transition, BNN has a large and anisotropic change in thermal expansion.[6,32] Abnormal grain growth can have many different origins, like compositional variety[46] or grain size distribution.[46] The exact reason for the abnormal grain growth is unknown, but because of the synthesis route it can not originate from density differences in the green body. The particle size distribution after milling was not measured or manipulated. Therefore, a broad distribution is a potential source and further experiments could manipulate the particle size distribution to remove it. A careful choice of sintering temperature and time was proven to be a successful method to circumvent the problem of abnormal grain growth in this project.

5.4.2 Microstructure and Sintering

Other compositions densify well at the applied sintering temperatures, resulting in small grains of comparable size and fairly high relative densities, as is seen in figure 4.5. The KBiN sample has the highest relative density and the least amount of visible pores. Taking into account that the fracture plane is the area in the ceramic with the highest density of pores, all other samples imaged have a good microstructure. There is still room for improvement and one could apply either a longer sintering time or increased sintering temperature to some of the samples. One example is for 0.4KBiN, where rounded grains can be seen in the SEM image. Even though this was not the focus of the master thesis, the observation is a

useful consideration for further research on the system.

5.4.3 Composition and Weight Loss

As seen in table 4.1, all samples lost some weight after sintering, compared to the powder used. It means that some of the species in the powder have evaporated during the sintering process. This affects the stoichiometry of the bulk material and shows that the sacrificial powder was not enough to protect the sample. To avoid this, more sacrificial powder could be used or the initial composition could be altered to take the evaporation of certain species into account.

In BNN, the sodium species has been shown by Jamieson *et al.* to deviate negatively from the general formula.[33] Some of the barium atoms have also been shown to occupy the cubic A1 site.[26,32] Assuming that all weight loss in BNN is due to sodium evaporation would give a composition of $Ba_4Na_{1.1}Nb_{10}O_{30}$. This is significantly lower than what is recorded by Jamieson *et al.*[33] and it is unlikely that only sodium contributes to the weight loss. The BNN rich samples of the solid solution tend to have higher weight loss and this is probably due to the increased sintering temperature. This will affect the content of KBiN, which has a lower melting temperature, the most. This could mean that the samples have a composition skewed slightly towards BNN. When assuming that most of the weight loss is due to evaporation of potassium and bismuth from KBiN, the uncertainty in composition could be as high as 0.06 in a worst case scenario. It is unlikely to be this high because other species would also evaporate. In addition, this uncertainty is only valid for the 0.2KBiN and 0.4KBiN solid solution compositions, because these have the highest weight loss, from which the uncertainty was calculated.

6 Conclusion

Six phase pure samples of BNN and KBiN solid solution with the tetragonal tungsten bronze structure were successfully synthesised. A density above 90 % was achieved for all samples with grains in the micrometer range. The KBiN rich side of the solid solution has a tetragonal structure, while the BNN rich side takes on the orthorombic Cmm2 space group at room temperature. From Pawley refinement of the x-ray diffraction patterns, a deviation from Vegard's law is observed in the evolution of both the a and c lattice parameters. A corresponding increase in peak dielectric permittivity confirms the placement of the morphotropic phase transition in the system at a composition of 0.6BNN-0.4KBiN. The critical temperature of both end members decrease with increasing solid solution, up to a composition of 0.5BNN-0.5KBiN. Broadened dielectric peaks and Uchino analysis of the dielectric data show that the solid solution exhibits relaxor like properties.

Abnormal grain growth was observed in BNN, but the origin of this has not been identified. Because of this, BNN samples proved more difficult to densify. BNN rich samples were also difficult to densify, due to significant weight loss as a result of sintering. This is likely caused by evaporation, primarily from KBiN, due to its lower melting temperature. Because of this, a possible deviation from the exact solid solution composition was calculated to be up to 0.06 for 0.8BNN-0.2KBiN and 0.6BNN-0.4KBiN.

Further Work

The increased dielectric permittivity achieved by solid solution of KBiN in BNN is a promising result. Despite this, the rapid decrease of the critical temperature towards room temperature is undesired. Other possible combinations of end members could be tested. One possibility is to swap the potassium atom in KBiN with a smaller atom like rubidium, or a larger one, like sodium. A larger atom could increase the critical temperature by stretching the O-Nb-O bonds, causing higher polarizability. [3]

Furthermore, to better pinpoint the MPB and increase the certainty of the study, other compositions with a narrower composition span can be synthesized, for instance the compositions 0.7BNN-0.3KBiN and 0.5BNN-0.5KBiN. Lastly, further investigation of the electrical properties of the samples should be performed. Measuring P-E hysteresis loops opens up for more ways to separate normal from relaxor behaviour, as there are some differences in how they appear in P-E hysteresis loops.

References

[1] M. Berger. Synthesis of Lead-free Ferroelectric Tetragonal Tungsten Bronzes. 2019.

[2] A. Magnéli. The Crystal Structure of Tetragonal Potassium Tungsten Bronze. *Arkiv för kemi*, 1:213–221, 1949.

[3] X. Zhu, M. Fu, M.C. Stennett, P.M. Vilarinho, I. Levin, C.A. Randall, J. Gardner, F.D. Morrison, and I.M. Reaney. A Crystal-Chemical Framework for Relaxor versus Normal Ferroelectric Behavior in Tetragonal Tungsten Bronzes. *Chemistry of Materials*, 27(9): 3250–3261, 2015. ISSN 08974756.

[4] The European Parliament and Council. Directive 2011/65/eu, 2011. URL `http://data.europa.eu/eli/dir/2011/65/2019-07-22`.

[5] S. S. Aamlid, S. M. Selbach, and T. Grande. The Effect of Cation Disorder on Ferroelectric Properties of $Sr_xBa_{1-x}Nb_2O_6$ Tungsten Bronzes. 2019. ISSN 1996-1944. doi: 10.3390/ma12071156.

[6] S. S. Aamlid, S. M. Selbach, and T. Grande. Structural Evolution of Ferroelectric and Ferroelastic Barium Sodium Niobate Tungsten Bronze. *Inorganic Chemistry*, 59(12):8514–8521, 2020. ISSN 0020-1669. doi: 10.1021/acs.inorgchem.0c00958.

[7] G. H. Olsen. Ferroelectric Tungsten Bronzes, 2016. ISSN 1503-8181. URL `http://hdl.handle.net/11250/2416836`.

[8] R. J. D. Tilley. *Understanding solids: the science of materials*. John Wiley & Sons, Ltd, 2nd edition, 2013. ISBN 9781118423462.

[9] A. R. West. *Solid state chemistry and its applications*. Wiley, Chichester, 2nd edition, 2014. ISBN 9781119942948.

[10] D. W. Richerson and W. E. Lee. *Modern ceramic engineering: properties, processing, and use in design*. CRC Press, Boca Raton, Fla, 4th edition, 2018. ISBN 9781498716918.

[11] I. B. Bersuker. On the origin of ferroelectricity in perovskite-type crystals. *Physics Letters*, 20(6):589–590, 1966. ISSN 0031-9163. doi: 10.1016/0031-9163(66)91127-9.

[12] K. Momma and F. Izumi. Vesta 3 for three-dimensional visualization of crystal, volumetric and morphology data. *Journal of applied crystallography*, 44:1272–1276, 2011. doi: 10.1107/S0021889811038970.

[13] R. Blinc. Order and disorder in ferroelectrics. *Ferroelectrics*, 301(1): 3–8, 2004. ISSN 0015-0193. doi: 10.1080/00150190490464845.

[14] W. Liu and X. Ren. Large Piezoelectric Effect in Pb-Free Ceramics. *Physical Review Letters*, 103(25):257602, 2009. doi: 10.1103/PhysRevLett.103.257602.

[15] B. Jaffe. *Piezoelectric ceramics*, volume 3 of *Non-metallic solids*. Academic Press, London, 1971. ISBN 0123795508.

[16] H. Fu and R. E. Cohen. Polarization rotation mechanism for ultrahigh electromechanical response in single-crystal piezoelectrics. *Nature*, 403 (6767):281–283, 2000. doi: 10.1038/35002022.

[17] P. Finkel, M. Staruch, A. Amin, M. Ahart, and S. Lofland. Simultaneous stress and field control of sustainable switching of ferroelectric phases. *Scientific Reports*, 5:13770, 2015. doi: 10.1038/srep13770.

[18] M. Ahart, M. Somayazulu, R. E. Cohen, P. Ganesh, P. Dera, H. Mao, R. J. Hemley, Y. Ren, P. Liermann, and Z. Wu. Origin of morphotropic phase boundaries in ferroelectrics. *Nature*, 451(7178):545–548, 2008. ISSN 1476-4687. doi: 10.1038/nature06459.

[19] D. Viehland, S. J. Jang, L. E. Cross, and M. Wuttig. Freezing of the polarization fluctuations in lead magnesium niobate relaxors. *Journal of Applied Physics*, 68(6):2916–2921, 1990. ISSN 0021-8979. doi: 10.1063/1.346425.

[20] A. A. Bokov, M. Maglione, A. Simon, and Z. G. Ye. Dielectric behavior of $Ba(Ti_{1-x}Zr_x)O_3$ solid solution. *Ferroelectrics*, 337(1):169–178, 2006. ISSN 0015-0193. doi: 10.1080/00150190600716747.

[21] P. Prelovsek and R. Blinc. Spin glass phase in mixed ferroelectric-antiferroelectric hydrogen bonded systems. *Journal of Physics C: Solid State Physics*, 15(27):L985–L990, 1982. ISSN 0022-3719. doi: 10.1088/0022-3719/15/27/008.

[22] K. Uchino and S. Nomura. Critical exponents of the dielectric constants in diffused-phase-transition crystals. *Ferroelectrics*, 44(1):55–61, 1982. doi: 10.1080/00150198208260644.

[23] R. Levit, J. C. Martinez-Garcia, D. A. Ochoa, and J. E. García. The generalized Vogel-Fulcher-Tamman equation for describing the dynamics of relaxor ferroelectrics. *Scientific Reports*, 9, 2019. ISSN 2045-2322. doi: 10.1038/s41598-019-48864-0.

[24] A. M. Glass. Investigation of the Electrical Properties of $Sr_{1-x}Ba_xNb_2O_6$ with Special Reference to Pyroelectric Detection. *Journal of Applied Physics*, 40(12):4699–4713, 1969. doi: 10.1063/1.1657277.

[25] J. Ravez and A. Simon. Some solid state chemistry aspects of lead-free relaxor ferroelectrics. *Journal of Solid State Chemistry*, 162(2): 260–265, 2001. ISSN 0022-4596. doi: 10.1006/jssc.2001.9285.

[26] V. M. Goldschmidt. Die Gesetze der Krystallochemie. *The Science of Nature*, 14(21):477–485, 1926. ISSN 0028-1042. doi: 10.1007/bf01507527.

[27] N. Wakiya, J. Wang, A. Saiki, K. Shinozaki, and N. Mizutani. Synthesis and dielectric properties of $Ba_{1-x}R_{2x/3}Nb_2O_6$ (r: rare earth) with tetragonal tungsten bronze structure. *Journal of the European Ceramic Society*, 19(6):1071 – 1075, 1999. ISSN 0955-2219. doi: 10.1016/S0955-2219(98)00376-8.

[28] J. E. Geusic, H. J. Levinstein, J. J. Rubin, S. Singh, and L. G. Van Uitert. The nonlinear optical properties of $Ba_2NaNb_5O_{15}$. *Applied Physics Letters*, 11(9):269–271, 1967. doi: 10.1063/1.1755129.

[29] S. Singh, D. Draegert, and J. Geusic. Optical and Ferroelectric Properties of Barium Sodium Niobate. *Physical Review B*, 2(7):2709–2724, 1970. doi: 10.1103/PhysRevB.2.2709.

[30] P. E. Tomaszewski. Structural phase transitions in crystals. I. Database. *Phase Transitions*, 38(3):127–220, 1992. doi: 10.1080/01411599208222899.

[31] G. Foulon, M. Ferriol, A. Brenier, G. Boulon, and S. Lecocq. Obtention of good quality $Ba_2NaNb_5O_{15}$ crystals: growth, characterization and structure of Nd^{3+}-doped single-crystal fibres. *European Journal of Solid State Inorganic Chemistry*, 33:673, 1996.

[32] M. Ferriol. Crystal growth and structure of pure and rare-earth doped barium sodium niobate (BNN). *Progress in Crystal Growth and Characterization of Materials*, 43(2-3):221–244, 2001. ISSN 0960-8974. doi: 10.1016/S0960-8974(01)00007-9.

[33] P. B. Jamieson, S. C. Abrahams, and J. L. Bernstein. Ferroelectric Tungsten Bronze-Type Crystal Structures. II. Barium Sodium Niobate $Ba_{(4+x)}Na_{(2-2x)}Nb_{10}O_{30}$. *The Journal of Chemical Physics*, 50 (10):4352–4363, 1969. doi: 10.1063/1.1670903.

[34] R. L. Barns. Barium Sodium Niobate ($Ba_{(4+x)}Na_{(2-2x)}Nb_{10}O_{30}$): Crystallographic Data and Thermal Expansion Coefficients. *Journal of Applied Crystallography*, 1:290, 1968.

[35] E. A. Giess, B. A. Scott, D. F. O'Kane, B. L. Olson, G. Burns, and A. W. Smith. Molten solution grown potassium sodium barium niobate crystals with a tungsten bronze-type structure. *Materials Research Bulletin*, 4(10):741–744, 1969. ISSN 0025-5408. doi: 10.1016/0025-5408(69)90064-6.

[36] I. G. Ismailzade. *Kristallografia*, 8(3):351, 1963.

[37] N. N. Krainik, V. A. Isupov, M. F. Bryzina, and A. I. Agranovskaya. Crystal Chemistry of Ferroelectrics With the Structural Type of Tetragonal Oxygen Tungsten Bronze. *Kristallografia*, 9(3):352–357, 1964.

[38] T. Sugai and M. Wada. Crystal Growth and Dielectric Properties of Potassium Bismuth Niobate. *Japanese Journal of Applied Physics*, 11 (12):1863–1864, 1972. doi: 10.1143/jjap.11.1863.

[39] Y. Li, C. Hui, Y. Li, and Y. Wang. Preparation of textured $K_2BiNb_5O_{15}$ ceramics with rod-like templates by the screen-printing technique. *Journal of Alloys and Compounds*, 509(23):L203 – L207, 2011. ISSN 0925-8388. doi: 10.1016/j.jallcom.2011.03.115.

[40] M. Shimazu, Y. Tanokura, and S. Tsutsumi. X-Ray Diffraction and Dielectric Studies on the $K_2BiNb_5O_{15}$-$K_2LaNb_5O_{15}$ System. *Japanese Journal of Applied Physics*, 28(Part 1, No. 10):1877–1881, 1989. ISSN 0021-4922. doi: 10.1143/jjap.28.1877.

[41] K. Kurbanov, E. S. Dosmagambetov, R. Ehlert, D. Schultze, and A. A. Kaminskii. Crystal growth and spectroscopic properties of Nd^{3+} ions in potassium bismuth niobate. *physica status solidi (a)*, 98(2): K175–K177, 1986. ISSN 0031-8965. doi: 10.1002/pssa.2210980257.

[42] G. H. Olsen, M. H. Sørby, S. M. Selbach, and T. Grande. Role of Lone Pair Cations in Ferroelectric Tungsten Bronzes. *Chemistry of Materials*, 29(15):6414–6424, 2017. ISSN 0897-4756. doi: 10.1021/acs.chemmater.7b01817.

[43] L. Vegard. Die Konstitution der Mischkristalle und die Raumfüllung der Atome. *The European Physical Journal A*, 5(1):17–26, 1921. ISSN 1434-6001. doi: 10.1007/bf01349680.

[44] R. D. Shannon and C. T. Prewitt. Effective ionic radii in oxides and fluorides. *Acta Crystallographica*, B25:925–946, 1969. doi: 10.1107/S0567740869003220.

[45] C. Wang. *Theories and Methods of First Order Ferroelectric Phase Transitions*. IntechOpen, 2010. ISBN 978-953-307-439-9. doi: 10.5772/13359.

[46] M. Hillert. On the theory of normal and abnormal grain growth. *Acta Metallurgica*, 13(3):227–238, 1965. ISSN 0001-6160. doi: 10.1016/0001-6160(65)90200-2.

Appendix A: SEM data

Additional SEM images of the samples are given in figure 6.1.

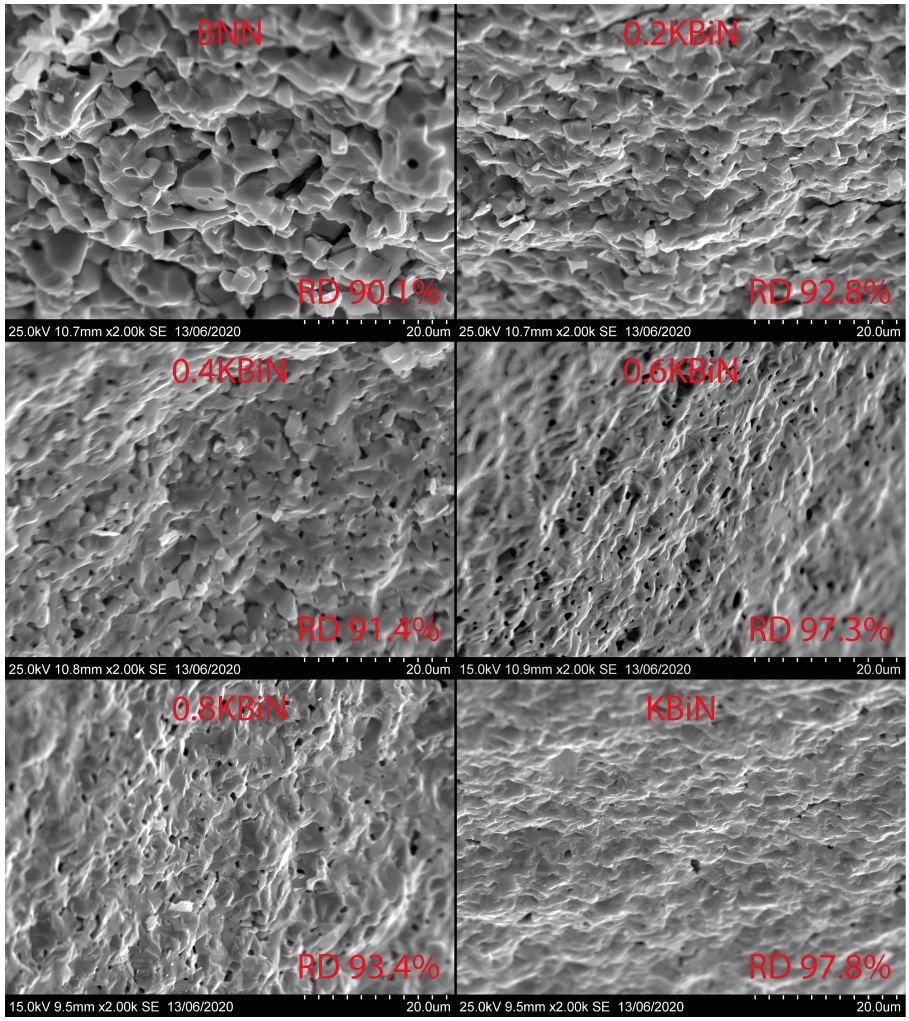

Figure 6.1: A zoomed in version of the SEM image of the microstructure of all samples shown in figure 4.5. RD denotes the relative density of the imaged samples. Notice that images have not been taken perpendicular to the fracture plane and that the image of BNN has a higher magnification.

Appendix B: XRD data

Zoomed in XRD spectra of all the different compositions with Pawley refinements are given in figure 6.2, 6.3, 6.4, 6.5, 6.6 and 6.7.

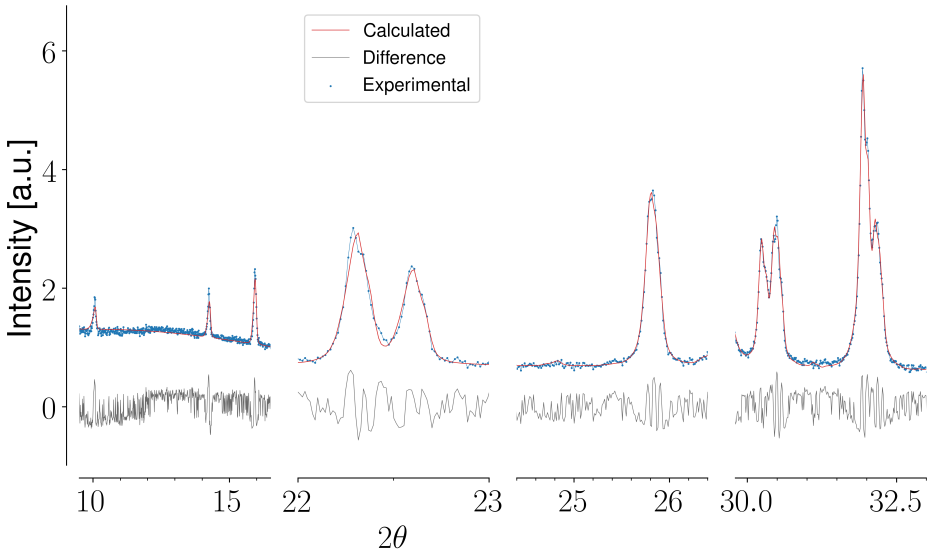

Figure 6.2: Pawley refinement of BNN diffractogram using the Cmm2 space group.

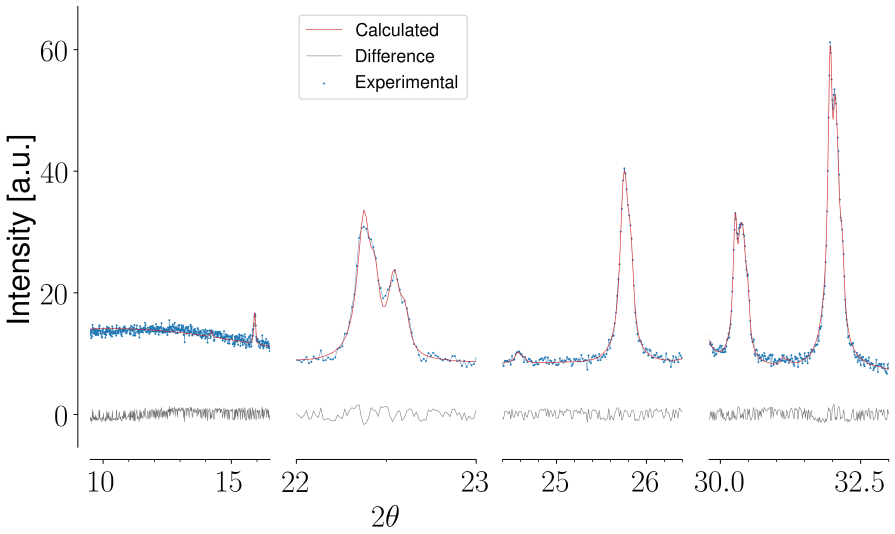

Figure 6.3: Pawley refinement of 0.2KBiN diffractogram using the Cmm2 space group.

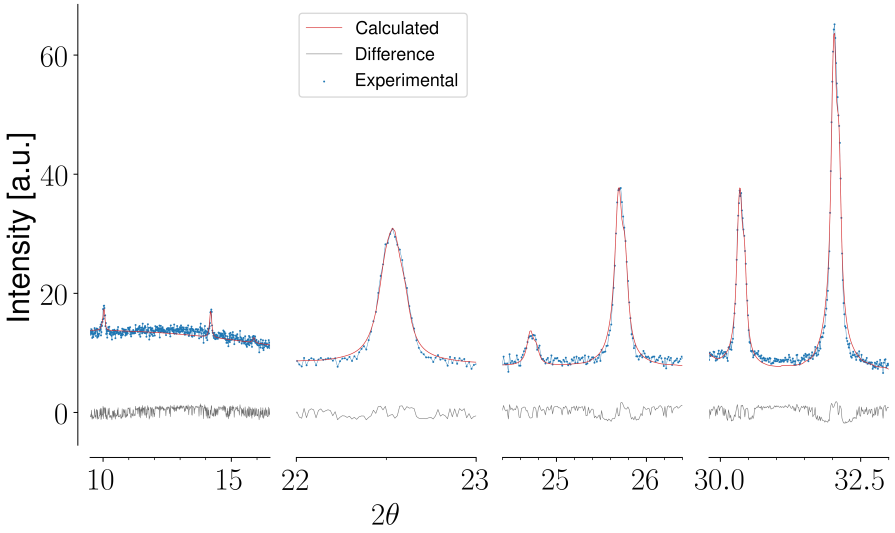

Figure 6.4: Pawley refinement of 0.4KBiN diffractogram using the Cmm2 space group.

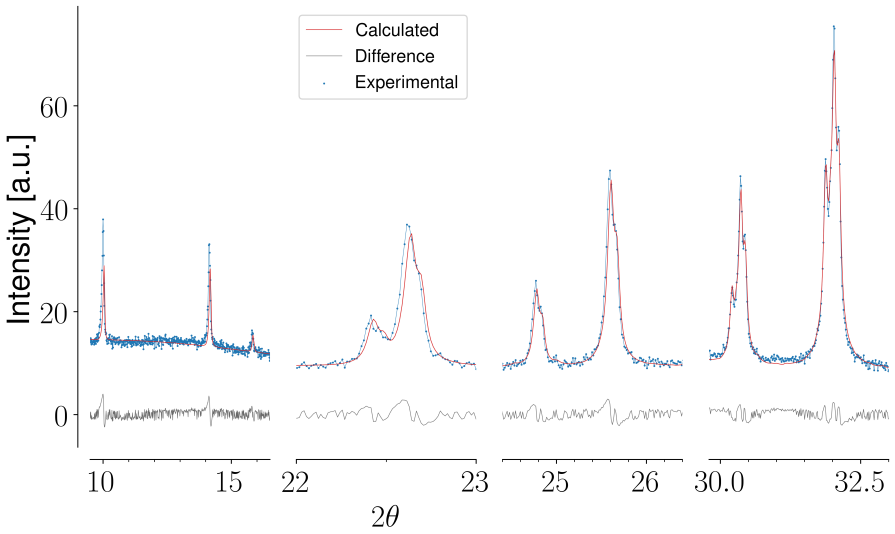

Figure 6.5: Pawley refinement of 0.6KBiN diffractogram using the P4bm space group.

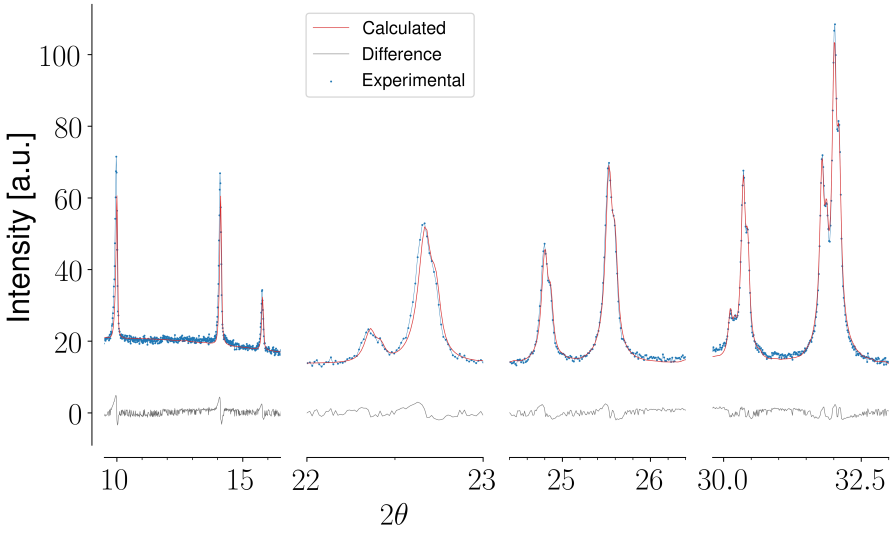

Figure 6.6: Pawley refinement of 0.8KBiN diffractogram using the P4bm space group.

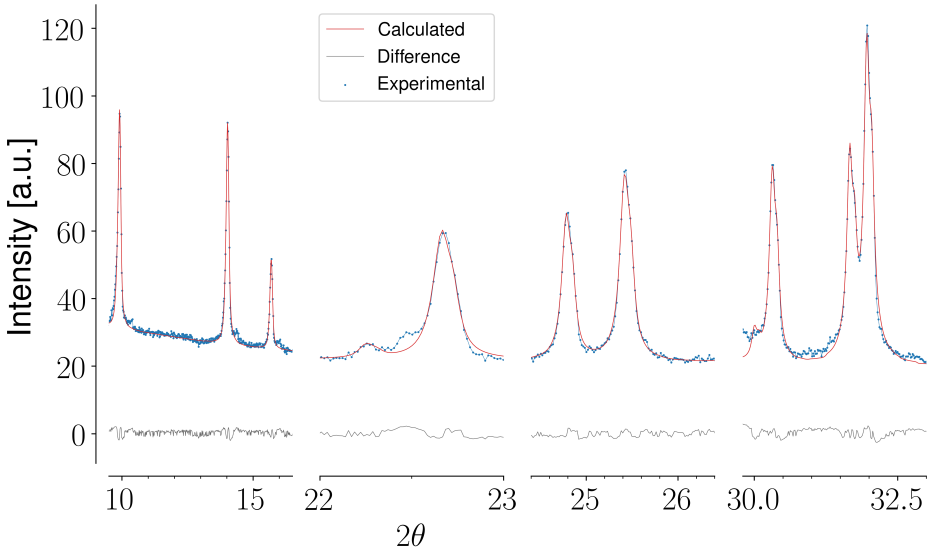

Figure 6.7: Pawley refinement of KBiN diffractogram using the P4bm space group.